Regulation of pH during enamel development

Jalali, R.

2017

document version
Publisher's PDF, also known as Version of record

Contents

Chapter 1

Introduction

Amelogenesis

Dental enamel is a specialized mineralized tissue that covers the crowns of the teeth and gives them the durability needed to withstand the forces of chewing. The process of enamel formation, or amelogenesis, results in the hardest biomineralized tissue consisting of 95% calcium hydroxyapatite [Ca10(PO4)6(OH)2] by weight with the remaining proportion consisting of protein and water (1). The cells that are responsible for formation of enamel are called ameloblasts and its formation occurs in two main stages. The first stage is the secretory stage during which ameloblasts are actively secreting proteins into the enamel space. At the end of this stage the final thickness of enamel is reached (2). The second stage of amelogenesis is the maturation stage. During this stage, the protein matrix is degraded by proteases and removed from the enamel space allowing the growth of hydroxyapatite crystals until the enamel reaches its final hardened state (2).

Secretory stage

When the first layer of dentin is formed, the newly differentiated ameloblasts start depositing the enamel matrix. Shortly after the secretory activity has started, the tall columnar ameloblasts develop at their apical (secretory) surface a single, fairly large cell process, called Tomes' process. The Tomes' process determines the orientation of the newly formed enamel matrix(3). The enamel matrix is composed of at least two major types of enamel-specific matrix proteins: amelogenins and enamelins (4). Amelogenins are proline-rich, hydrophobic, proteins making up approximately 90% of the enamel matrix proteins(5). Experimental inhibition of amelogenin translation results in interference of crystal growth, thus indicating the importance of this protein for generating full-width enamel (6). The general idea is that amelogenins are capable of binding to the apatite surface and modulate hydroxyapatite formation by reducing crystal outgrowth (7, 8). Another possible function of amelogenins is that they act as a buffer to neutralize the protons, generated during crystal formation (2, 9). However, the mechanisms by which amelogenins influence crystal growth remains elusive. Enamelins are acidic, hydrophilic glycoproteins, considerably larger than amelogenins. They are mainly attached to the hydroxyapatite crystallites and continue to be present in the mature enamel. They are thought to act as crystal nucleators in forming enamel, resembling in their action the acidic phosphoproteins in bone and dentin (10).

Maturation stage

Once the enamel crystallites have reached their final length, the Tomes' processes retract and ameloblasts begin to modulate between a cell type with a flat apical plasma membrane (smooth- ended) and one in which that membrane formed multiple invaginations (ruffle-

ended) (11). The latter stage marks their entrance into the maturation stage. After most of the matrix (specifically the amelogenins) and the fluid have been removed, the mineral component increases steeply from 10-20% to 80-90% as a percentage of volume (12). The most unique aspect of the maturation stage is the cyclical and rapid morphological change in ameloblasts between "ruffle-ended ameloblasts" (RA) and "smooth-ended ameloblasts" (SA) (2, 11). The smooth-ended ameloblasts contain tight junctions at their basal pole while the ruffle-ended ameloblasts have these junctions at their apical pole restricting ion movement between the cells into the enamel (summarized in Fig.1) (13). This cyclical change from ruffle-ended into smooth- ended cells allows bidirectional diffusion of small peptides and ions into/out the enamel layer (14, 15). In this stage the ameloblasts do not have any significant protein synthesizing organelles such as Golgi and rough ER (2) but contain a significant number of energy-providing mitochondria (16). This supports the aforementioned concept that at this stage the primary function of these cells is to actively transport the ions and molecules back and forth rather than any significant synthesis of new molecules. The ameloblast layer also connects with gap junctions to the adjacent layer (papillary layer), assumed for direct transport of small molecules and ions between both layers that form a functional unity (17). Expression of membrane proteins such as $Na^{+/}K^{+}$-ATPase in the papillary layer indicate that this layer possibly contributes to ion/ molecules transport to the enamel matrix, via ameloblasts, and maintenance of the intracellular ionic environment of the ameloblast-papillary layer complex (18, 19).

Mineralization of the enamel

The mineralization of the enamel begins immediately after secretion of the matrix by secretory ameloblasts and continues during the maturation stage of amelogenesis. Calcium required for mineralization enters the ameloblasts via calcium entry channels (SOCE, ACEC) and calcium is sequestered in the endoplasmic reticulum (20). Ca^{2+} has been proposed to diffuse through the endoplasmic reticulum, via SERCA2 as the main Ca^{2+} refilling pump, is released into the distal cytoplasm and extruded into the enamel space via Ca-ATPase pumps, Na^{+}-Ca^{2+} exchangers and Na^{+}-K^{+}-Ca^{2+} exchangers (18, 21). Phosphate transport possibly occurs by a sodium-phosphate cotransporter (18).

Factors that (may) impair the function of ameloblasts

Possible etiological factors which may impair the function of ameloblasts could be categorized as genetic and exogenous factors.

(1) *Genetic factors*. More than a hundred genes are potentially involved in amelogenesis. The protein products of these genes regulate gene expression needed for ameloblast function. Thus, it is not surprising that 25-80% of the human population suffers from enamel defects

(22). For some of these candidate genes a mutation was shown to cause structural defects in the enamel including amelogenesis imperfecta (AI) (23), characterized by a variety of developmental enamel defects including hypoplasia and hypomineralization. Knockout mice lacking genes such as kallikrein-4 (tooth specific protease), Slc4a2(Ae2) and CFTR exhibited multiple anomalies including enamel defects (24-26)

(2) *Exogenous factors*. Ameloblasts are sensitive to toxic effects of the environment (local or systemic) especially during the first 6 years of life, the time period that crowns of all permanent teeth (except 3rd molars) develop. The effects of external factors leave lasting defects in the structure of enamel that do not heal like other tissues in the body. A well-known external factor influencing ameloblast function during amelogenesis is fluoride when it is ingested in excessive amounts during childhood (27). Other factors such as infection, trauma, irradiation, chemicals, nutrition deficiencies and metabolic disorders have been shown to influence ameloblast function during amelogenesis as well (28-30).

Rodent model to study the enamel defects

The effects of both genetic and exogenous factors have been studied in animal species, especially in rodents. The continuously erupting rodent incisor has been used as a model system that throughout life forms enamel and dentin, allowing to examine in detail the effects of gene mutations or external factors on each separate stage of amelogenesis in a single sagittal section, even in adult animals. Amelogenesis in these animals, in particular rat and mouse, is well mapped (1). Small rodents have been proved to be also a good model for studying the effect of exogenous factors such as fluoride on enamel development, since they show the same fluorotic mineralization defects at the same range of plasma fluoride levels as in humans (31).

Model to study pH regulation by ameloblasts

The pH values of forming enamel are maintained near neutral during secretion stage; however, they show considerable variation during maturation stage, shifting from acidic (pH 6.0-6.2) to neutral values and then rising to slightly higher levels in more mature enamel. In recent years, evidence showed that maturation ameloblasts express a set of membrane-spanning and cytosolic proteins that are typical for ion-transportation and pH-regulation during enamel development in other transport epithelia as in kidney, colon and pancreatic tubular epithelia (21, 26, 32, 33). Many of these membrane transporters/channels have already been described in other organs such as the kidney and intestine. Fig 2 compares a model for ion transport by intestinal epithelium (summarized in Fig.2a) with proposed ion transport by ameloblasts (summarized in Fig.2b). The similarity between both models suggests that ameloblasts use many of the same transporters/channels to secrete bicarbonate to control pH in enamel. The known pH regulation pathways to date employed by

ameloblasts in the enamel organ involve (1) Carbonic anhydrase (mainly CA2 and CA6) to generate bicarbonate, (2) Chloride ion exchangers and channels to exchange chloride ions across the apical plasma membrane, (3) Bicarbonate cotransporter to permit the passage of bicarbonate from external sources, across the basal end to the apical pole of the ameloblasts, and (4) Na^+/ H^+ exchangers to remove H^+ ions generated during intracellular production of bicarbonate (14, 18, 25, 34). Based on the abnormal phenotypes resulting from the lack of expression of the genes and proteins associated with these pathways, it has been proposed that the development of enamel requires maintenance of pH at all stages of enamel formation.

Hypothesis and thesis outline

In this thesis we focused on the possibility that ameloblasts buffer protons during maturation stage of amelogenesis. We hypothesized that (1) ameloblasts express a set of different ion transporters/exchanger(s) to secrete bicarbonates similar as typical transport epithelia to neutralize the protons released during crystal formation in the enamel space; and (2) insufficient neutralization of the protons released during the formation of enamel in mice with null mutation of pH regulators are responsible for formation of hypomineralized immature enamel.

In **Chapter 2**, we investigated the possible involvement of Ncbe1 (Slc4A2), a member of the solute carrier family (SLC4A) family of ion-transporters, to regulate intra- and extracellular pH in eukaryotic cells by cotransporting HCO3- and Na+. In order to secrete bicarbonate directly into the enamel space, anion exchangers or cotransporter(s) for bicarbonates need to be localized in the apical plasma membrane (or secretory pole) of polarized ameloblasts. Candidate transporters in maturation ameloblasts are various members of the solute carrier (Slc) family 26A, including Slc26a3/Dra, Slc26a6/Pat1, and Slc26a4/Pendrin. Previously, our group showed that Pendrin is expressed in ameloblasts but is not critical for enamel formation (33). In **Chapter 3**, we examined whether maturation ameloblasts express two other members of this family Dra and Slc26a6 and the effect of null mutation of these regulators on enamel structure in mouse models.

Accumulation of Na^+ and K^+ in the hypomineralizing enamel suggested that maturation ameloblasts transport both types of ions into enamel and but remove these from the enamel space by yet unknown mechanisms (18). Potential transporters capable of reabsorbing K^+ and Na^+ reabsorption belong to the Na^+:K^+:$2Cl^-$ (NKCC) cotransporter family. In **Chapter 4**, we therefore examined whether mouse maturation stage ameloblasts express Na^+:K^+:$2Cl^-$ cotransporter (NKCC1) involved in ion transport.

In **Chapter 5**, we tested the hypothesis that enamel fluorosis in human teeth is associated with insufficient neutralization of the extra protons released during exposure of

developing enamel to fluoride. This concept was suggested by animal experimental studies in which fluoride caused formation of hypermineralization lines (35). In this chapter, we tested whether this concept was also true for human enamel by examining whether human fluorotic teeth contain hypermineralized lines.

Finally, we discuss our major findings in **Chapter 6** and propose a more complete model on the role of different ion exchangers/transporters during enamel development.

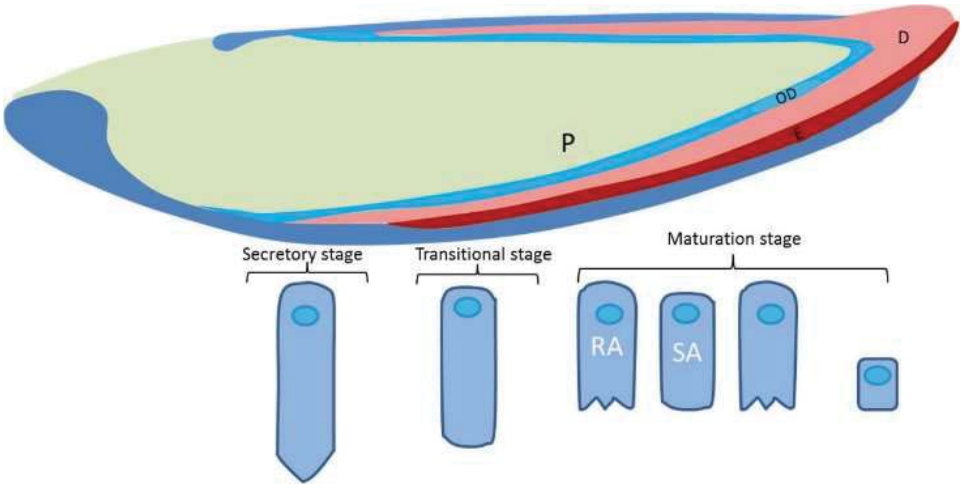

Fig 1. Ameloblast changes during enamel formation. The figure represents secretory, transition and maturation stage ameloblasts in rodent, respectively. During the secretory stage, ameloblasts develop a secretory specialization. At this stage ameloblasts secrete proteins at a mineralization front where the enamel crystals grow in length. At the end of the secretory stage, the enamel has achieved its final thickness. During the transition stage, the ameloblasts undergo a major restructuring that diminishes their secretory activity and changes the types of proteins secreted. KLK4 and MMP20 are the major proteases secreted, which degrade the accumulated protein matrix. During the maturation stage ameloblasts modulate between ruffled (RA) and smooth-ended (SA) phases. Their activities harden the enamel layer by promoting the deposition of mineral in to the enamel matrix.
P, pulp; OD, odontoblast; D, dentine; E, enamel.

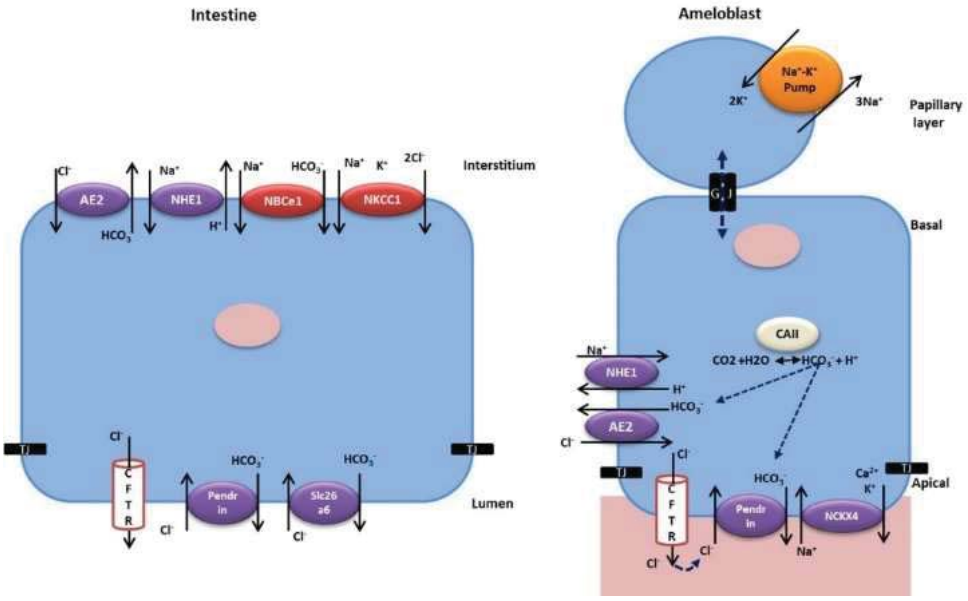

Fig 2. Comparison of location and possible ion transport of transepithelial transporters in intestine epithelium and ameloblasts. (A) intestine cell. At the basolateral pole, $HCO3^-$ is regulated by NBCe1 and at the apical pole by SLC26 family (Pendrin and Slc26a6). In ameloblast (B), $HCO3^-$ formed by CAII activity may be extruded via Pendrin or another anion exchanger(s) into the enamel space. In both ameloblasts and intestine Cl^- is extruded by CFTR and exchanged by Slc26a6 for $HCO3^-$. Function of a variety of other transporters such as AE2 and NHE1 in ameloblasts is the same as in intestine and indicate the importance of other ions for the proper function of the ameloblasts. Ca^{2+} needed for hydroxyapatite formation maybe transported out of the cells at the apical pole by at least one of the NCKX members of sodium- calcium-potassium exchangers (NCKX4) (18, 36)

Chapter 2

NBCe1 (SLC4A4) a potential pH regulator in enamel organ cells during enamel development in the mouse

Jalali R, Guo J, Zandieh-Doulabi B, Bervoets TJ, Paine ML, Boron WF, Parker MD, Bijvelds MJ, Medina JF, DenBesten PK, Bronckers AL. NBCe1 (SLC4A4) a potential pH regulator in enamel organ cells during enamel development in the mouse. Cell Tissue Res. 2014: 358(2):433-442 .

ABSTRACT

During formation of dental enamel maturation-stage ameloblasts express ion-transporting transmembrane proteins. The SLC4 family of ion-transporters regulates intra- and extracellular pH in eukaryotic cells by cotransporting $HCO3^-$ with Na^+. Mutation in SLC4A4 (coding for the Na^+ bicarbonate cotransporter NBCe1) induces developmental defects in human and murine enamel. We hypothesized that NBCe1 in dental epithelium is engaged in neutralizing protons released during crystal formation in the enamel space. We immunolocalized NBCe1 protein in mouse wild-type dental epithelium and examined the effect of *NBCe1*$^{-/-}$ mutation on enamel formation in mice. Ameloblast expressed gene transcripts for *NBCe1* isoforms B/D/C/E. In wild-type mice weak to moderate immunostaining for NBCe1 that recognizes isoforms A/B/D/E and isoform C was seen in secretory ameloblasts, no or very low staining in early maturation stage ameloblasts but moderately to high staining in late maturation stage ameloblasts. The papillary layer showed the opposite pattern and immunostained prominently at early maturation stage but gradually showed less staining at mid- and late maturation-stage. In *NBCe1*$^{-/-}$ mice ameloblasts were disorganized, the enamel thin and severely hypomineralized. Enamel organs of *CFTR*$^{-/-}$ and *AE2a,b*$^{-/-}$ mice (believed to be pH regulators in ameloblasts) contained higher levels of NBCe1 protein than wild-type mice. Our data show that expression of NBCe1 in ameloblast and papillary layer cell depends on developmental stage and possibly responds to pH changes.

INTRODUCTION

Enamel formation is a unique process of cell-regulated biomineralization that occurs in two stages: secretory phase characterized by the initiation of enamel crystals and their slow extension in length, and maturation stage during which crystals rapidly expand in width and thickness (2). The development of enamel requires tight control of pH at all stages of formation (37, 38). The formation of hydroxyapatite crystals produces large quantities of protons that need to be buffered to sustain mineralization (2). It is believed that in secretory stage, amelogenins play an important role in buffering pH but that in maturation stage after removal of amelogenins other mechanisms operate (39). A recent report proposed that maturation stage ameloblasts secrete protons to keep the surface free from mineral (14). A majority of studies however is in favor for the concept that ameloblasts secrete bicarbonate to buffer protons released by mineral formation (33, 37, 40), either in response to or independent from extracellular acidification (41).

Ameloblasts express a series of (mostly) transmembrane proteins typical for pH regulation and ion transport in epithelia (thyroid, non-acid secreting cell of the collecting ducts of kidney and pancreatic ducts). These proteins include several types of carbonic anhydrase (most abundantly types 2 and 6), the cystic fibrosis transmembrane conductance regulator (CFTR), the electrogenic sodium-bicarbonate cotransporter-e1 (NBCe1), the electroneutral sodium bicarbonate cotransporter 1 (NBCn1) and anion exchanger -2 (AE2) (21).

The electrogenic Na^+: $HCO3^-$ cotransporter NBCe1, encoded by SLC4A4 is a member of the SLC4A (solute carrier bicarbonate transport) family (38, 42, 43). SLC4A4 has three major variants, two N-terminally spliced (NBCe1-A and NBCe1-B), and one C-terminally spliced variant, (NBCe1-C) as well as several minor variants (D and E). Mutation of NBCe1 in human results in developmental defects in kidney, leading to acidosis (proximal renal tubular acidosis), and changes in eyes and teeth (21, 44, 45). *NBCe1*$^{-/-}$ mice have a severe and fatal phenotype, die before weaning (37, 44) and have "chalk white" enamel that easily fractures. The detection of transcripts of *NBCe1*-B and immunostaining of enamel organs of wild-type mice showed that NBCe1 operates locally in dental epithelium (14, 40, 46). The enamel organ contains several cell types but which of these tissues synthesize which isotypes was not clear and antisera were not well specified (14, 40, 46). The function of Nbce1 in dental epithelium is also not yet clear, but could potentially be involved in pH regulation. The *NBCe1* gene of murine ameloblast-like cells contains a pH responsive element in its promoter region(47) and *NBCe1* gene expression of mouse ameloblast-like cell increased when culture medium was acidified to pH 6.0(40), a value reached in vivo in enamel below ruffle-ended ameloblasts during pH cycling (48).

The aims of the present study were (1) To record the expression of Nbce1 protein in

enamel organ at all stages of enamel development; (2) To determine changes in structure of ameloblasts and enamel mineralization in teeth from *NBCe1*$^{-/-}$ mice and (3) To test whether ameloblasts *in vivo* respond to pH changes *in situ* by enhancing Nbce1 expression. For this we used two other mouse models in which pH regulation is severely disrupted which severely affects enamel formation: the *AE2a,b*$^{-/-}$ (25) and *CFTR*$^{-/-}$ mice (26).

MATERIALS AND METHODS

Animals and tissues

Tissues were collected from wild-type mice 12-18 days old, 3-6 month old (adult) mice, hamsters (4-8 days old) and 9-12 weeks old rats (adult). After sacrifice complete upper and lower jaws were dissected as well as soft tissues as stomach, brain and kidney. Homozygous *NBCe1* $^{-/-}$ and heterozygous tissues were collected from *NBCe1* $^{-/-}$ mice at 14 days of age. The targeting procedure (44) replaced sequences that include part of exon 9 (amino acids 421-455, LNIQA....TDNMQ including 3'splice site) of the kidney variant and part of intron 9 with a neomycin resistance gen, removing the C-terminal portion of Nbce1 downstream from exon 9. Tissues and tissue sections from *AE2a,b* $^{-/-}$ and *CFTR*$^{-/-}$ mice were from previous studies (25, 26). All animal handling complied with national and international regulations for Animal Care and permission was obtained from the Committee for Animal Care.

Polymerase chain reaction

Fresh tissues were collected and mRNA extracted as reported (26). Table 1 presents the primers details primers to detect different transcripts for NBCe1.

Antibodies

In rat NBCe1 consists of 1079-1094 amino acid residues and contains an N-terminal cytoplasmic domain of 428-468 amino acid residues, a 521 amino acid residue transdomain with as many as 14 transmembrane segments and a cytoplasmic C–terminus domain with 90-105 amino acid residues.

Two different polyclonal antibodies to NBCe1 were raised in rabbits using maltose-binding protein (MBP) fusion protein system (49). The first one (antiserum K1A) was raised against recombinant-produced peptide fragment coding for the C- terminal 46 amino acids of rat brain (DCPYSEKVPSIKIPMDITEQQPFLSDNKPLDRSSTFLERHTSC) and reacts with the NBCe1-A/B/D/E isoforms. The rat NBCe1-A/B is 96% identical to NBCe1 from human pancreas and heart. The second antibody (antiserum B1B) was raised to the last 61 C-terminal amino acids present in and specific for the NBCe1-C isotype (EKDPQHSLNATHHADKIPFLESLGLPSPPRSPVKVVPQIRIELESEDNDYLWRNKGT ETTL). In negative controls primary antisera were replaced by non-immune normal rabbit

sera. Kidney and brain were used as positive controls, and specificity of the antisera was tested by staining sections from jaws from *NBCe1*$^{-/-}$ mice.

Immunostaining

Paraffin sections were dewaxed in xylene, rehydrated in a descending series of ethanol, and rinsed in phosphate buffered saline and immunostained with peroxidase–technique using an Envision Kit (DakoCytomation, Denmark) with primary antibodies diluted 1:200-1:400. After washing, the peroxidase conjugates were visualized with 3,3′-Diaminobenzidine tetrahydrochloride (DAB) substrate (to produce a brown end-product; Envision Kit; DakoCytomation, Glostrup, Denmark) or with 3-Amino-9-ethylcarbazole (AEC) substrate (to produce a red end-product; Invitrogen) for 10 min at room temperature according to the manufacturer's instructions, and counterstained with hematoxylin or methyl green.

Western blotting

From freeze-dried wild-type, *CFTR*$^{-/-}$ and *AE2a,b*$^{-/-}$ mice early maturation stage enamel organs mice were microdissected incisally from an imaginary reference line between M1 and M2 indicating the border between secretory and maturation stage. The apical half of the maturation stage enamel organ was removed by micodissection, dissolved under non-reducing condition in SDS loading buffer (from Nucleospin Triprep kit) and protein was measured using the BCA protein assay (Bio-Rad, Hercules, CA). Five to 10 µg of non-denatured protein were loaded on SDS PAGE in a 3-8% Tris acetate Nupage gel with Tris acetate as running buffer for 60 min at 150 V and electroblotted by an iBlot device (Invitrogen) on nitrocellulose membrane according to the manufacturer's instructions. Based on the prestained protein markers (Novex sharp protein standards; Invitrogen), blots were horizontally cut into two parts just above the 50-kDa prestained marker. The upper part, with protein was probed with either one of the rabbit NBCe1 antiserum (1:100). The lower part was probed with β-actin monoclonal mouse antibody (Sigma) with a dilution of 1:10,000. IRDye 800CW conjugated goat anti-rabbit IgG (H+L) highly cross-adsorbed (LI-COR; Product number: 926-32211) and IRDye 680CW conjugated goat anti-mouse IgG (H+L) highly-cross adsorbed (LI-COR; Product number: 926-32220) were applied as a second antibody for 90 minutes at room temperature (1:5000, LI-COR) prior to washing with phosphate buffered saline (PBS). Visualization and quantification was carried out with the LI-COR OdysseyH scanner and software (LI-COR Biosciences). Red color (for actin) was detected at 680 nm wavelength and a green color (for NBCe1) was detected at 800 nm wavelength. For quantification we used Odyssey software. Values were normalized for actin and expressed as percentage of wild-type (100%).

Microcomputed tomography

To determine the degree of mineral content, freeze-dried, MMA-embedded hemimaxillae from three 14-days old *NBCe1*$^{-/-}$ mice and three wild-type or heterozygous mice were scanned at resolution of 8µm voxel using a Micro-CT-40 high resolution scanner (Scanco Medical,AG, Bassersdorf, Switzerland). Mineral density was determined at sequential stages of development. Cross-sectional virtual images were collected from most developed (incisor tip) to the least developed (cervical area). The most incisal slice containing the most mineralized enamel was identified visually, and the mineral density [mg HA/ cm^3] measured at 3 sites in enamel, dentin and surrounding bone and values averaged per slice. Measurements were made at 100 micrometer intervals and slices at the same developmental stage from three mice per group averaged and plotted as function of stage (slice number). An independent t-test was used to compare the groups. Statistical significance was set at $p < 0.05$.

RESULTS

Gene transcripts and NBCe1 protein in ameloblasts

Transcripts for NBCe1-B/C/E (no further distinction, first primer set), isoform D/E (second primer set) and isoform C (third primers set) were detected in enamel organ of mouse incisors (Fig. 1). Incisors and developing molars gave positive immunostaining with both antisera in the dental epithelium of hamsters (Fig. 2a-c, 3h), mice (Fig. 2d-j) and rats (Fig 3a-g) depending on the stage of amelogenesis. In the cervical loop the first weak staining for NBCe1-A/B/D/E was seen in stratum intermedium, later appeared in early secretory ameloblasts and increased gradually (Fig. 2a,2d). In secretory ameloblasts staining was diffuse intracellular and often confined to a sharp line at the base of the Tomes processes that disappeared during transitional stage (Fig. 2b-2d, Fig. 3a). The papillary layer stained strongly with both antisera (Fig. 2c, 2e-g, 3b) while the underlying ameloblast layer was almost negative in early maturation stage.

At the mid maturation stage, ameloblasts started to stain again and staining intensity increased to late maturation stage while a gradual reduction of staining was noticed in the regressing papillary layer (Fig. 2g-j, 3c, e-g). Staining in maturation stage ameloblasts was intracellular and in basolateral plasma membranes (Fig. 2i). In maturation stage the positive-stained layer of ameloblasts contained occasionally small groups of unstained or weakly stained cells (possibly smooth-ended cells; Fig c,d) while the adjacent papillary layer was immunopositive (Fig. 2j)

Both antisera gave a similar staining pattern, both in incisors and developing molars (Fig. 3h). Antiserum to NBCe1-A/B/D/E was more consistent than the anti-NBCe-1C which gave more background. Both antisera also gave positive staining in nuclei of some cells in transitional, mid- and late maturation stage (Fig. 2i and 3f), more frequently seen in antiserum

to NBCe1-C (Fig. 3f). Extracellular enamel was also positive but when primary antiserum was replaced by non-immune sera it stained as well.

Specificity of the employed NBCe1 antisera was validated by staining incisors from *NBCe1*$^{-/-}$ mice. The strong intracellular staining and staining associated with the membranes was lost but in a variable and weak overall staining remained (Fig 3i), similar as obtained when primary antisera were replaced by non-immune sera. Also in tissues derived from *NBCe1*$^{-/-}$ mice the nuclei of some cells of the papillary layer reacted with the antisera, indicating that this staining was non-specific.

Reduced enamel mineralization in NBCe1$^{-/-}$ *determined by micro-CT*

Three-dimensional reconstructions of micro-CT images showed that the surface of molar and incisor enamel was smooth and without defects in control mice (Fig 4a–d) but rough and irregular in *NBCe1*$^{-/-}$ mice (Fig. 4e–h).

Mineral density in maxillary incisors of *NBCe1*$^{-/-}$ mice plotted as function of developmental stage was lower than in control enamel, and failed to increase in maturation stage (Fig 4i) In *NBCe1*$^{-/-}$ mice the mean mineral density of enamel was 59% of control value and for dentin 89% while mineral density in bone was not changed (Fig. 4j).

Histological changes in enamel organ in NBCe1$^{-/-}$ *mice*

In contrast to well polarized ameloblasts formed in wild-type mice, ameloblasts of *NBCe1*$^{-/-}$ mice lost polarity, became short and round as reported (37). The enamel matrix was not homogenous, irregular, and thin and an additional structureless enamel layer had deposited on top of normally structured layer. Cellular organization of odontoblast and dentin layer was indistinguishable between wild-type and *NBCe1*$^{-/-}$ mice.

Upregulation of NBCe1 protein in enamel organ of AE2a,b$^{-/-}$ *and CFTR*$^{-/-}$ *mice*

Western blotting of maturation stage ameloblasts using anti-NBCe1-A/B/D/E (Fig. 5d green bands, K1A antibody), or anti-NBCe1-C (Fig. 5e green bands, antiserum B1B) showed a major broad band between 110 kD and 160kD, corresponding with the posttranslational modified 120 kD NBCe1.

To investigate whether NBCe1 was involved in buffering of forming enamel and reacted to the higher acidity of the enamel matrix, due to proton release during mineral accretion we immunostained enamel organs from *AE2a,b*$^{-/-}$ and *CFTR*$^{-/-}$ mice with antisera to NBCe-1 to examine an attempt to compensate for defective pH regulation by enhancing NBCe1 production as for instance seen in cholangiocytes in *Ae2a,b*$^{-/-}$ mice (50). In enamel organs of *AE2a,b*$^{-/-}$ mice the ameloblasts stained more intense and early maturation stage

ameloblasts turned immunopositive sooner than in controls (Fig. 5a,b). This effect was more dramatic in enamel organs of *CFTR*$^{-/-}$ (Fig. 5c). On western blots of enamel organs NBCe1 protein was 4.3 fold higher in *AE2a,b*$^{-/-}$ (not significant) and 11.3 fold higher in *CFTR* $^{-/-}$ ($p<0.05$) in comparison with wild-type controls (Fig. 5j)

DISCUSSION

Intracellular immunostaining for NBCe1 was previously reported to be present in secretory ameloblasts of mouse and human incisors (40, 46), and in the rat in maturation stage papillary layer but not in maturation stage ameloblasts (14). We show here that the synthesis of NBCe1 protein depends on the developmental stage and changes with time and location. During secretion stage ameloblasts stained weakly to moderately, virtually lost staining at early maturation stage but restained at mid- and late maturation stage. Gaps of negative immunostaining seen in small groups maturation stage ameloblasts - also seen for by immunostaining for AE2a,b (25, 51) suggest that during maturation stage some ameloblasts apparently cease production of NBCe1 and/or rapidly digest it to restart biosynthesis a short time later. These changes in production of NBCe1 may reflect differences in activity between smooth- ended and ruffle-ended ameloblasts.

It has been reported that mouse ameloblasts and immortalized murine ameloblast-like cells (LS8) express NBCe1-B but not NBCe1-A or NBCe1-C (37, 40, 46). We report here that mouse ameloblasts express transcripts for NBCe1-B/D/E, NBCe1-D/E and NBCe1-C. Antiserum to NBCe1-A/B/D/E reacted strongly with dental epithelial cells indicating that NBCe1-isoform B and/or D/E isoforms are translated. Also the antiserum specific to NBce1-C stained dental epithelium positive, essentially in a similar pattern. Enamel organ cells apparently produce various isoforms simultaneously. The differences in outcome between our present and previous data (46) and data (37, 40) that ameloblasts do not express NBCe1-C isoform may be explained by the use of different primer sets.

In a recent paper some of us reported expression of NBCe1-A fetal human ameloblasts (46). This however appeared to be incorrect by use of the wrong primer set for the human tissues as pointed out recently (38).

NBCe1 is a bidirectionally operating electrogenic transmembrane ion-transporter which can cotransport 1 bicarbonate for 2 or 3 Na^+, either in or out the cell depending on cell type and the concentration gradient over the plasma membrane. The enhanced production of NBCe1 in maturation ameloblasts of *CFTR*$^{-/-}$ and *AE2ab*$^{-/-}$ mice suggests that these cells responds to changes in pH in the forming enamel by enhancing NBCe1 synthesis to compensate for the dysfunctioning of AE2a,b and CFTR. Whether the various NBCe isotypes have the same function at different stages of amelogenesis is not clear. The opposite immunostaining patterns for NBce1 seen between maturation ameloblasts and papillary layer

suggest both layers can cooperate with each other in dealing with pH and may pass small ions through the gap junctions between both cell types (14). The very high protein expression of NBCe1 in papillary layer and the fact that NBCe1 cannot compensate for absence of functional CFTR and AE2 suggests that NBCe1 primarily regulates intracellular pH in the papillary layer cells.

NBCe1 cotransports 1 Na^+ with 2–3 bicarbonates which requires a Na^+ gradient over the plasma membrane. Conceivably, the low intracellular Na^+ that this cotransport needs is accomplished by the activity of Na^+, K^+-ATPase in plasma membranes of the papillary layer (14, 19, 52) continuously pumping out 3Na+ and importing $2K^+$. In addition, other, yet unknown mechanisms must be operating in enamel organ cells to compensate for charge differences that result from increased negative charge when NBCe1 and Na^+-K^+ exchangers are functional.

The absence of functional NBCe-1 in ameloblasts in *NBCe1*$^{-/-}$ mice does not rule out that also systemic changes as low bicarbonate levels in blood and renal acidosis contribute to development of enamel defects.

In conclusion, ameloblasts express different isoforms of NBCe1 including isoform B/D/E/ and/or D/E and isoform C. Ameloblasts cells need functional NBCe1 to sustain mineral accretion likely to buffer protons. Ameloblasts and papillary layer cells are complementary in expressing NBCe1 and likely closely cooperate to regulate pH.

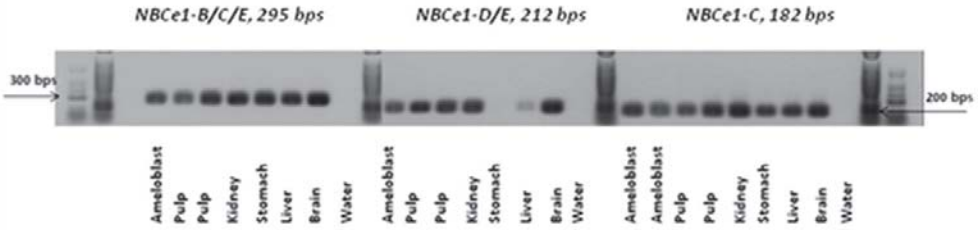

Fig.1 . Transcipts for NBCe1 variants in mouse tissues (PCR)

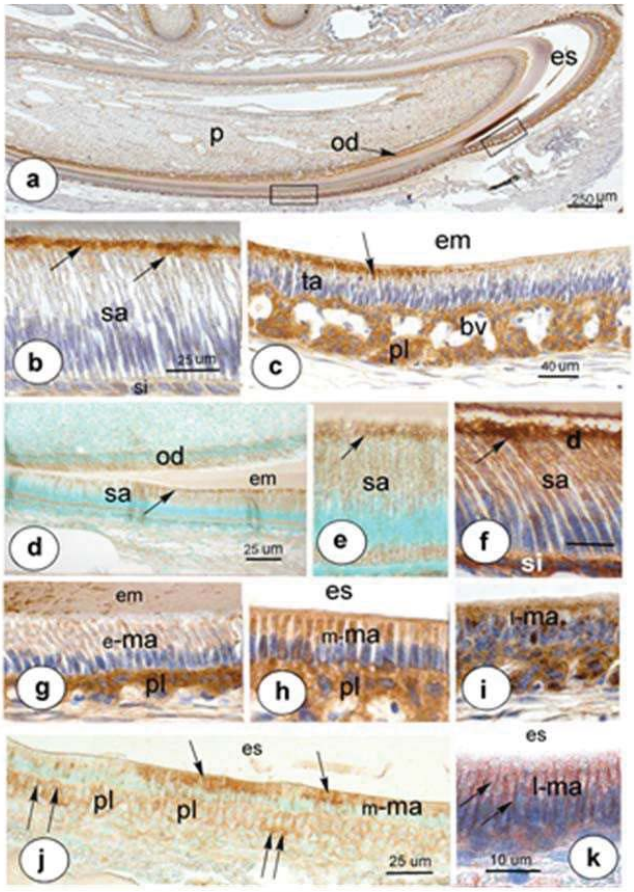

Fig 2. Immunostaining for NBCe1-A/B/D/E in developing hamster (a-c) and mouse (d-k) mandibular incisors. Progressive development from left (cervical loop) to right (incisal end). (a): boxed areas enlarged in (b and c). Arrows point at immunopositive apical line at the base of Tomes process that disappears at transitional stage. (g): early maturation ameloblasts (e-ma), (h): mid maturation ameloblasts (m-ma) and (i) late maturation ameloblasts. Note some nuclei are immunopositive. (j) shows groups of positive stained ameloblasts (single arrows) separated by negative ameloblasts. Adjacent papillary cells have the opposite pattern (double arrows). (k) positive staining in/near lateral membranes (arrows) of late maturation ameloblasts (peroxidase staining with AEC, red). BV blood vessels, ma maturation ameloblasts, sa secretion ameloblasts; od odontoblasts; pl papillary layer; es enamel space; em enamel matrix; si stratum intermedium. (d,e and j) counterstained with methylgreen; all others with heamatoxylen

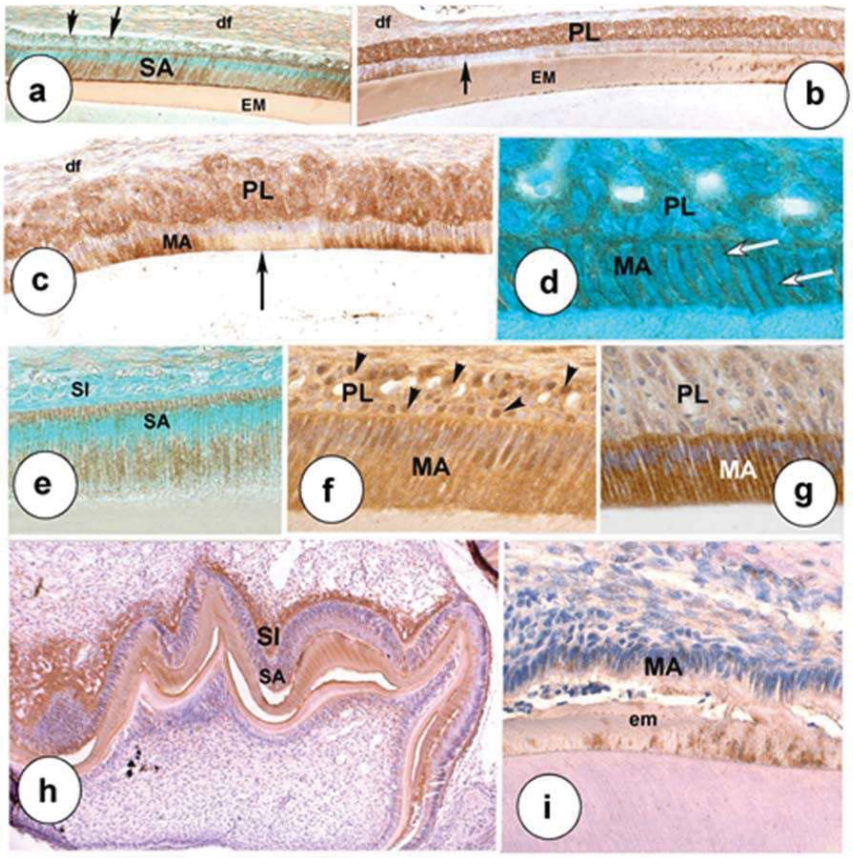

Fig. 3. NBCe1 staining in developing maxillary teeth stained with anti-NBCe1-A/B/D/E (a-d, h, i) and anti-NBCe-1C (e,f,g). (h) hamster molar, all other rat incisors. (a): Secretion stage with positive staining ameloblasts (SA), outer enamel epithelium (arrow) and stratum intermedium (SI). (b): arrow indicates negative staining in transitional ameloblasts but strong staining in papillary layer (PL). (c) gap of negative staining at late maturation (arrow).Fig 3d. Basolateral staining (arrows) in late maturation ameloblasts. (e) virtual lack of staining in stratum intermedium (SI) secretory ameloblasts positive; (f) staining in maturation ameloblasts and nuclei in papillary layer (arrow heads). (g) Mid- late maturation stage ameloblast, papillary layer barely stained. (h) staining in stratum intermedium of a molar tooth germ. (i) *NBCe1*$^{-/-}$ mouse stained with anti NCBce1-A/B/D/E. SA secretory ameloblasts , SI stratum intermedium, PL papillary layer, df dental follicle, em enamel matrix . Magnification*400

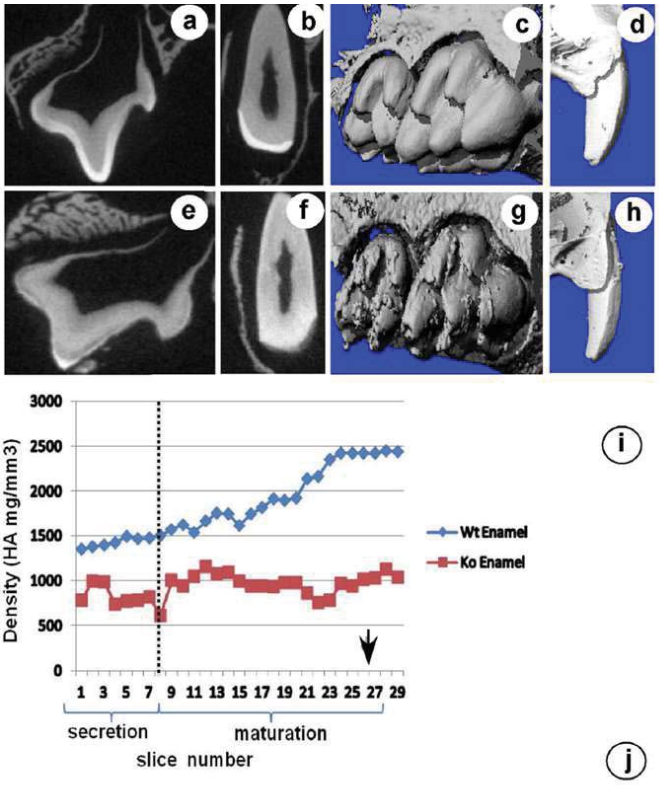

Effect of NBCe1$^{-/-}$ on Mineral Density of Enamel, Dentin and Bone

Density (HA mg/mm3)	Groups			p value
	NBCe1$^{+/+}$	NBCe1$^{-/-}$	treated/control	
Enamel	2236 ± 334	1335± 81	59%	0.01
Dentin	1392 ± 35	1241± 34	89%	<0.01
Bone	1005 ± 49	1012± 28	100%	0.85

Fig.4. Micro-Ct images of cross-sections through maxillary incisors and molars in a digital reconstruction of a wild-type and an *NBCe1*$^{-/-}$ (14 days old). Enamel in the *NBCe1*$^{-/-}$ mutant mouse is poorly mineralized (e,f,i). Table 1 illustrates that enamel and dentin mineral content of *NBCe1*$^{-/-}$ animals is significantly lower than that of controls ($p<0.05$) (j). Bone density did not differ between wild-type/heterozygous littermate controls and *NBCe1*$^{-/-}$ mice assessment in micro-CT ($p>0.05$)(j). Values are mean SD. Independent t-test was used to compare the groups.

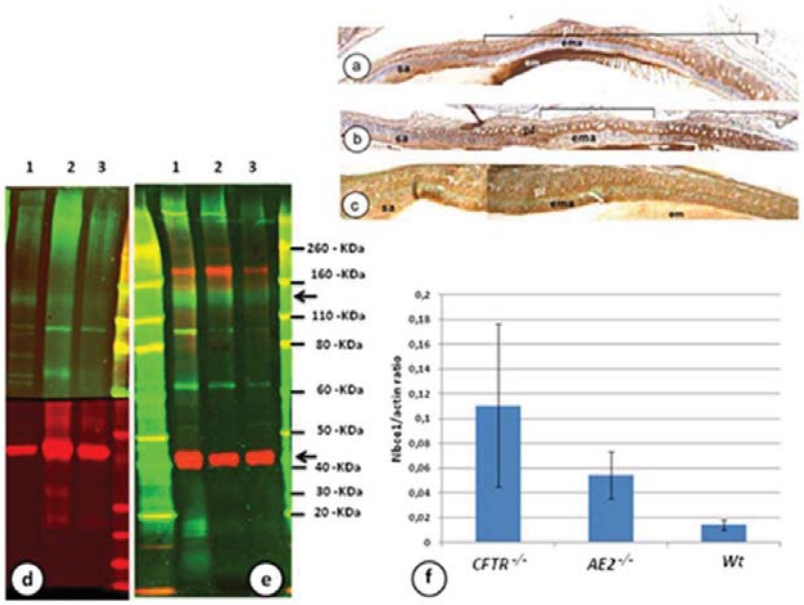

Fig. 5. Immunostaining for NBCe-1 on tissue sections (a-c) and western blots (d-f) from enamel organs from wild-type (wt), *CFTR*$^{-/-}$ (''ko'') and *AE2a,b*$^{-/-}$ (''ko'') mice. A negative gap of NBCe1-A/B/D/E staining early maturation ameloblasts in wild-type mice (a, bracket) is shortened in *AE2a,b*$^{-/-}$ mice (b) or absent in *CFTR*$^{-/-}$ mice (c). (d-e): western blot of enamel organ extracts from *CFTR*$^{-/-}$(lane 1), *AE2a,b*$^{-/-}$(lane 2) and wild-type mice (lane 3) stained with anti-NBCe1-A/B/D/E (d) or with anti-NBCe-1C serum (e). NBCe-1 staining in green, actin (43 kD) in red. Both antisera revealed a dominant immunoreactive band between 110 and 160 kD (arrow) corresponding to the predicted molecular weight of the parent NBCe1 120 kD, strongly upregulated in *CFTR*$^{-/-}$ and *AE2a,b*$^{-/-}$ mice. (f) illustrates that NBCe1 (main band) /actin ratio in enamel organs of *CFTR*$^{-/-}$ mice is significantly higher than that of controls (11.3 fold, mean and SD, n=3; $p<0.05$). NBCe1/actin ratio in *AE2a,b* $^{-/-}$ was increased 4.3-fold but did not reach statistical significance.

Table 1. Primer sequences for PCR variants of NBCEe1/SLC4A4 in wild-type mice

Gene variant	Gene Bank access number	Position	Primer sequence	Annealing tempearture oC	Product size (bps)
SLC4A4 isoforms B,C,E (kidney/pancreas variant)	NM_001197147	FW(58-79) REV (352-331)	5' CCCAGGAGGATGGAGGATGAAG 3' 5' AGATGAATCGGATGCGTTCTGC 3'	58	295
SLC4A4 isoforms D and E (kidney/pancreas variant)	NM_001197147	FW (604-623) REV(785-768)	5' CCACAGCTGGTGGAGATGAT 3' 5' GTCATGGCTGGGCTGCTT 3'	63	182
SLCA44 isoform C (brain variant)	NM_001136260	FW(3147-3167) REV (3358-3337)	5' GGATAGCGACAATGACGATGA 3' 5' AAACAGGTTACAACGTGGTTTC 3'	63	212

Chapter 3

SLC26a3/Dra and Slc26a6 in murine ameloblasts

Jalali R, Zandieh-Doulabi B, DenBesten PK, Seidler U, Riederer B, Wedenoja S, Micha D, Bronckers AL. Slc26a3/Dra and Slc26a6 in Murine Ameloblasts. J Dent Res. 2015;94(12):1732-9.

ABSTRACT

Formation of apatite crystals during enamel development generates protons. To sustain mineral accretion, maturation ameloblasts need to buffer these protons. The presence of cytosolic carbonic anhydrases, the basolateral Na^+ bicarbonate cotransporter Nbce1, and the basolateral anion exchanger Ae2a,b in maturation ameloblasts suggests that these cells secrete bicarbonates into the forming enamel, but it is unknown by which mechanism. Solute carrier (Slc) family 26A encodes different anion exchangers that exchange $Cl^-/HCO3^-$, including Slc26a3/Dra, Slc26a6, and Slc26a4/pendrin. Previously, we showed that pendrin is expressed in ameloblasts but is not critical for enamel formation. In this study, we tested the hypothesis that maturation ameloblasts express Dra and Slc26a6 to secrete bicarbonate into the enamel space in exchange for Cl^-. Real-time polymerase chain reaction detected mRNA transcripts for Dra and Slc26a6 in mouse incisor enamel organs, and Western blotting confirmed their translation into protein. Both isoforms were immunolocalized in ameloblasts, principally at maturation stage. Mice with null mutation of either Dra or Slc26a6 had a normal dental or skeletal phenotype without changes in mineral density, as measured by micro–computed tomography. In enamel organs of *Slc26a6*$^{-/-}$ mice, Dra and pendrin protein levels were both elevated by 52% to 55%. The amount of Slc26a6 protein was unchanged in enamel organs of *Ae2a,b*$^{-/-}$ and *CFTR*$^{-/-}$ mice but reduced in Dra$^{-/-}$ mice by 36%. Our data show that ameloblasts express Dra, Pendrin, or Slc26a6 but each of these separately is not critical for formation of dental enamel. The data suggest that in ameloblasts, Slc26a isoforms can functionally compensate for one another.

INTRODUCTION

Ameloblasts form enamel in 2 stages: a secretion stage, in which they secrete a protein-rich matrix primarily consisting of amelogenins, and a maturation stage, during which most of these proteins are degraded and removed from the enamel space. Simultaneously, mineral is deposited in an ordered pattern. Formation of apatite mineral releases protons into the enamel matrix microenvironment, which could acidify the enamel compartment (21, 37). During the secretory stage, mineral accretion is low, and the pH may in part be regulated by amelogenins, shown to have a high buffering capacity (53). During maturation, however, the rate of mineral formation increases (9), and removal of amelogenins from the enamel compartment implies the necessity for enamel matrix pH to be regulated by other mechanisms. Various studies support the idea that ameloblasts secrete bicarbonate into the enamel space via transmembrane proteins (2). Hypomineralization of dental enamel and changes in the structure of enamel seen in mice with defective or dysfunctional cystic fibrosis transmembrane conductance regulator (CFTR;(45)), basolateral anion exchanger 2 (Ae2; (25)), and Na^+ bicarbonate cotransporter Nbce1 (54, 55) support the concept that ameloblasts are involved in secreting bicarbonates (37). The molecular mechanisms responsible for actually secreting bicarbonate into the enamel space is unknown, but it likely is an anion exchanger located in the apical membrane facing the forming enamel.

The solute carrier (SLC) gene family comprises ~55 gene families that contain ~360 protein- coding genes (56), several of which have been detected in ameloblasts (14, 25, 26, 33, 37, 40, 44). Previous studies have shown that in other epithelial cells, the chloride channel CFTR is functionally involved in pH regulation. Mutation of CFTR affects many cell types, including sweat glands, intestine, bile ducts, pancreatic ducts, respiratory epithelia, submandibular glands, uterus, and vas deferens (57-60). These studies suggested 2 possible functions for CFTR: transport of Cl^- and regulation of the activity of other $Cl^-/HCO3^-$ transporters (61, 62). Therefore, by conducing Cl^- imported from interstitial tissue fluid by basolateral Ae2 in exchange for intracellular bicarbonate (37), CFTR provides the enamel space with Cl^- that can be exchanged for bicarbonates mediated by anion exchangers in the apical membranes. The SLC family A26 (SLC26A) encodes multifunctional anion exchangers that transport a wide range of substrates, including Cl^-, $HCO3^-$, sulfate, oxalate, and formate (63).

SLC26A members that exchange $Cl^-/HCO3^-$ include SLC26A3/DRA (downregulated in adenoma), SLC26A4 (Pendrin), and SLC26A6 (putative anion transporter 1; (63)). The mouse Dra protein consists of 575 amino acids, whereas Slc26a4 and Slc26a6 are each 780 amino acids long (86 kDa). Slc26a4 is predominantly expressed in the thyroid, inner ear, and kidney (64); Slc26a6, in both kidney and the gastrointestinal tract (65, 66); and Dra, in the mucosa of the lower intestinal tract, apical membranes of columnar epithelium,

and pancreatic ducts (67). Homozygous mutations in DRA cause congenital chloride diarrhea (68), whereas mutation in SLC26A6 causes hyperoxaluria, hyperoxalemia, and calcium oxalate urolithiasis (69).

We showed that secretory- and maturation-stage mouse ameloblasts express Slc26a4 (Pendrin). However, disruption of this gene presented no dental phenotype possibly by compensation by other Slc26a members (33). Ameloblasts resemble pancreatic ductal epithelium that expresses various Slc26a members (Dra and Slc26a6) to secrete bicarbonates (62). In this study we addressed 2 questions: (1) Do mouse ameloblasts express Dra and Slc26a6? (2) Is there compensation between different Slc26a family members that could explain why *Pendrin*$^{-/-}$ mice, for example, have no dental phenotype?

To test this, the enamel organs of mice were analyzed for expression of Dra and Slc26a6 at the protein level. The effect of the null mutation of both isoforms on enamel development and their potential compensation by changes in Dra and Slc26a6 expression was studied by micro–computed tomography and Western blotting in *Dra*$^{-/-}$ and *Slc26a6*$^{-/-}$ mice. In various types of transport epithelia, the transport activity of Slc26A isotypes depends on functional CFTR, so we also determined whether the amount of Slc26a6 protein was changed in *CFTR*$^{-/-}$ ameloblast.

MATERIAL AND METHODS

Animals

Tissues were collected from adult *Dra*$^{-/-}$ mice (129S6/SvEv mouse strain; (70)) and *Slc26a6*$^{-/-}$ mice (strain of 129/SvJ mouse phage library kindly donated by Dr. P. Aronson, Yale University, New Haven, CT, USA;(69)) and wild-type control littermates. After sacrifice, lower jaws and several other soft tissues were excised, slam-frozen and freeze-dried, or fixed for immunohistochemistry according to a standard protocol and shipped to Amsterdam for processing and analysis. Details on these mutant mice have been published elsewhere ((69, 70). Briefly, *Slc26a6*$^{-/-}$ mice were generated by replacing exons 1 and 2 and part of exon 3 in the Slc26a6 gene by a Neo gene cassette. *Dra*$^{-/-}$ mice were generated by inserting a Neo cassette into exon 2 of the Dra gene. Mouse enamel organs with a null mutation in *Ae2a,b* and *CFTR* and 6- to 8-d-old wild-type mice were from previous studies (25, 26). All animal handling complied with national and international regulations for animal care, and permission was obtained from the Committee for Animal Care of Abteilung Gastroenterologie; Medizinische Hochschule Hannover (Hannover, Germany), and Department of Medicine, University of Yale (New Haven, CT, USA).

Histological procedures

For immunohistochemistry, tissues from *Slc26a6*$^{-/-}$ and control mice (n = 3 in each) were fixed in 4% formaldehyde in 0.1M phosphate buffer at pH 7.4 overnight, decalcified in 10% EDTA containing 0.8% formaldehyde at pH 7.4 for 6 week at room temperature, embedded in paraffin, and sectioned. Mandibles from *Slc26a3/Dra*$^{-/-}$ and *Slc26a6*$^{-/-}$ mice and wild-type littermates were scanned by micro–computed tomography prior to decalcification.

Real-time quantitative Polymerase Chain Reaction (rT-QPCR)

Total RNA was extracted from tissues with the NucleoSpin RNA/Protein Kit (Macherey-Nagel, Düren, Germany) according to the manufacturer's instructions. First-strand cDNA synthesis was performed in a 20-µL reverse transcription (RT) reaction containing 200 ng of total RNA via the VILO Kit (Invitrogen, Bleiswijk, Netherlands) according to the manufacturer's instructions. Real- time polymerase chain reaction (PCR) analysis was used to analyze mRNA expression of *Dra* and *Slc26a6* and the housekeeping protein tyrosine 3-monooxygenase (YWHAZ) with the primer sequences shown in the Appendix Table by using the LightCycler 480 system based on SYBR Green I dye (Roche Applied Science, Indianapolis, IN, USA). The LightCycler reactions were prepared in 20 µL of total volume with 7 µL of PCR-H2O, 0.5 µL of forward primer (0.2 µM), 0.5 µL of reverse primer (0.2 µM), 10 µL of LightCycler Mastermix (LightCycler 480 SYBR Green I Master; Roche Applied Science), to which 2 µL of cDNA (5 times diluted) was added as PCR template. Controls in the real-time RT PCR reaction included RT reactions without the reverse transcriptase (control for DNA carryover) and RT reactions without template (control for reagent contamination). With the LightCycler software, the crossing points were assessed from a standard curve of 5 serial dilutions ranging from 10 ng to 1.6 pg of cDNA. PCR efficiency (E) was automatically calculated with the fit point method (E = 10–1/slope). Gene expression data were used only if the PCR E was within a range of 1.85 to 2.0. From each gene, the amount of measured DNA was normalized to that of the YWHAZ housekeeping gene to calculate relative gene expression.

Immunohistochemical staining

Paraffin sections were dewaxed in xylene, rehydrated in a descending series of ethanol, and rinsed in phosphate-buffered saline (PBS). The following antisera were used:

1) mouse monoclonal anti-Dra (H0001811-M01; Abnova, Taipei, Taiwan) against a peptide corresponding with amino acid sequence 503 to 600 of mouse Dra (TQFPKCSTLANIGRTNIYKNKKDYYDMYEPEGVKIFRCPSPIYFANIGFFRRKLIDA VGFSPLRILRKRNKALRKIRKLQKQGLLQVTPKGFICTVDT);

2) rabbit anti-Dra (Research Genetics, Huntsville, AL, USA) against the synthetic peptide FNPSQEKDGKIDF, corresponding to amino acids 731 to 744 of the human SLC26A3/DRA cDNA (GenBank L02785.1)—this antiserum was further purified on a protein G minicolumn;

3) affinity-purified rabbit anti-Slc26a6 against a peptide (DLRRRDYHMERPLLNQEHLEE) of the N- terminal domain of human SLC26A (donated by Dr. P. Aronson, Yale University, New Haven, CT, USA; and

4) affinity-purified rabbit anti-Pendrin (Slc26a4; SC-50346, H-195; Santa Cruz Biotechnology, Tebu-Bio, Heerhugowaard, Netherlands; (33, 71)).

Antigen retrieval was performed either in 10mM citrate buffer (pH 6.0) at 60 °C overnight or for 20 min in microwave at 95 °C prior to staining or by a mild predigestion with a proteinase K solution (10 μg/mL; in PBS) for 15 min at 37 °C. After retrieval, endogenous peroxidase was inactivated with a peroxidase block solution (Envision Kit; DakoCytomation, Carpinteria, CA, USA) for 5 min. Sections were washed in 0.1M TBS (Tris-buffered saline; 0.9% NaCl, pH 7.2) containing 0.1% bovine serum albumin. To prevent nonspecific staining, sections were incubated for 30 min with 2% bovine serum albumin in PBS. Sections were then incubated overnight at 4 °C with primary antibodies or with matched nonimmune IgG (1 to 2 μg/mL) or normal serum (1:100 to 1:200) to serve as controls. Prior to incubation of mouse tissues with primary mouse antibodies, sections were incubated with mouse-on-mouse blocking kit (HistoMouse BEAT Blocker Kit; Invitrogen). After overnight incubation at 4 °C with primary antibodies, sections were washed 3 times in TBS and incubated 1) with goat-anti rabbit IgG antibodies conjugated with peroxidase polymer and rabbit anti mouse IgG conjugated with peroxidase polymer (Envision kits) for 1 h at room temperature and counterstained with hematoxylin or 2) with goat anti rabbit–Alexa Fluor 488 (5 μg/mL; Invitrogen) 1 to 2 h at room temperature and counterstained with DAPI (Vector Laboratories, Burlingame, CA, USA)

Western blotting

From freeze-dried mandibular incisors, enamel organs at early maturation stage from wild-type and null mutant mice were microdissected incisally from a reference line projected between M1 and M2 to make a distinction between secretory and maturation stages. The apical half of the enamel organ was dissected, dissolved under nonreducing condition in SDS loading buffer (from NucleoSpin TriPrep kit), and protein was measured with the BCA protein assay (Bio-Rad, Hercules, CA, USA). Five to 10 μg of kidney and colon denatured protein or 20 to 30 μg of enamel organ denatured protein were loaded on SDS-PAGE in a 3% to 8% Tris acetate NuPAGE gel (ThermoFisher Scientific, Grand Island, NY, USA) with Tris acetate as running buffer for 60 min at 150 V and electroblotted by an iBlot device

(Invitrogen) on nitrocellulose membrane according to the manufacturer's instructions. Blots were incubated with rabbit primary antibodies (1:200 antibodies) and mouse-β-actin antibody (1:1,000; Sigma, St. Louis, MO, USA) overnight. IRDye 800CW conjugated goat anti-rabbit IgG (H+L) highly cross-adsorbed (926-32211; LI-COR Biosciences, Lincoln, NE, USA) and IRDye 680CW conjugated goat anti-mouse IgG (H+L) highly cross-adsorbed (926-32220; LI-COR) were applied as a second antibody for 90 min at room temperature (1: 5,000; LI-COR) prior to washing with PBS. Visualization and quantification were carried out with the OdysseyH scanner and software (LI-COR). Red color (for actin) was detected at a 680-nm wavelength, and a green color (Slc26A members) was detected at a 800-nm wavelength. For quantification, Odyssey software was used. Intensity values of the bands were normalized for actin and expressed as percentage of wild-type (100%).

Micro-computed tomography (micro-CT)

To determine mineral density, hemimandibles from 16-wk-old mouse mutants and littermate wild-type controls were scanned at 55 kV, 145-µA beam intensity, 8-µm image pixel size, with a microCT-40 high-resolution scanner (Scanco Medical AG, Bassersdorf, Switzerland). Mineral density was determined at sequential stages of development. An internal standard made of solid- sintered apatite (5-mm diameter, 1.5 to 2.0 mm thick, solid sintered) with density of 2.9 ± 0.2 g/mL (a gift from Himed; http://www.himed.com) was used as high-density standard. Cross-sectional virtual images were collected from the most developed (incisor tip) to the least developed (cervical area; Fig. 4a). The slice at the incisor tip containing the most highly mineralized enamel was identified visually. Measurements in enamel were made halfway between enamel surface and enamel-dentin junction at 500-µm intervals (50 slices at 10-µm interval), at 3 sites per slide, averaged, and calculated per developmental stage per mouse. Group averages (3 mice/group) were calculated and plotted as function of stage (slice number). Independent t test was used to compare the groups. Statistical significance was set at $P < 0.05$.

RESULTS

Real time Quantitative PCR

PCR analysis based on mouse-specific primers confirmed that mRNA transcripts for *Dra* were detectable in enamel organ, liver, brain, and stomach (Fig. 1a). Transcripts for Slc26a6 were detectable in enamel organs, dental pulp, brain, liver, tongue, colon, and stomach (Fig. 1b).

Immunodetection and immunolocalization of Slc26a3/Dra and Slc26a6 in developing teeth

On western blots characteristic bands between 70-110 kDa immunoreactive with anti-Dra and anti-Slc26a6 were identified in enamel organ extracts of wild-type mice. Failure to stain these bands in *Dra*$^{-/-}$ and *Slc26a6*$^{-/-}$ tissue validated the specificity of the antibodies (Fig. 1c)

Weak fine-granular intracellular staining for Dra was noted in secretory ameloblasts (Fig. 2a), as well as strong intracellular staining with preference over the apical membranes in maturation ameloblasts (Fig. 2b, c). Ameloblasts of *Dra*$^{-/-}$ and *Slc26a6*$^{-/-}$ mice did not stain with their respective antibodies (only shown for *Dra*$^{-/-}$ ameloblasts) (Fig. 2d). Staining for Slc26a6 was granular and weak in the secretory stage, increased at late secretory stage (Fig. 2e), and strong in the maturation stage ameloblasts (Fig. 2f) concentrating apically (Fig. 2g). The papillary layer was positive in early and mid-maturation, but staining was low at late maturation stage (Fig. 2f, g). When primary antibodies were replaced by nonimmune serum or matching nonimmune IgG, cells did not stain (Fig. 2h), except occasionally over extracellular matrices, especially in undecalcified sections or tissues that were incompletely decalcified.

Analysis of enamel formation in Dra$^{-/-}$ *and Slc26a6*$^{-/-}$ *mice*

No anatomical changes were observed in incisors (or molars) of *Dra*$^{-/-}$ and *Slc26a6*$^{-/-}$ mice; incisors had the usual orange pigment, contained a sharp edge and showed no excessive wear.

Micro–CT analysis showed that the mineral density in both mutant strains was not different from their wild-type littermate controls (Fig. 3). Histologic evaluation showed no apparent changes in ameloblast or enamel structure in mutant mice.

Changes in protein levels for Slc26a isoforms in Dra$^{-/-}$ *and Slc26a6*$^{-/-}$ *ameloblasts*

To examine whether in ameloblasts the members of Slc26a family could compensate for one another, we tested maturation stage enamel organs from null mutant tissues for changes of expression of the nonmutated isoforms by Western blotting (Fig. 4). Maturation stage ameloblasts from *Dra*$^{-/-}$ mice stained with anti-Slc26a6 (Fig. 4) showed a 36% decrease of staining intensity compared with wild-type littermate controls ($P = 0.015$). In *Slc26a6*$^{-/-}$ mice, staining for Dra and Pendrin/Slc26a4 had increased by 52% ($P = 0.01$) and 55% ($P = 0.002$), respectively. Enamel organs of *Ae2a,b*$^{-/-}$ mice stained for Dra (Fig. 4), and Slc26a6 showed no quantitative change in protein expression. In *CFTR*$^{-/-}$ ameloblasts, Slc26a6 protein tended to be enhanced, but this was not statistically significant (Fig. 4; $P = 0.10$).

DISCUSSION

In the present study, we examined the expression by, and the potential role of, Dra and Slc26a6 in ameloblasts during formation of dental enamel. We detected immunoreactive protein bands of the predicted sizes for both transporters in enamel organs of wild-type mice but not in enamel organs of null-mutant mice. We found that the apical border of maturation ameloblasts stained positive with anti-Slc26a6 and anti-Dra, similar as found for Pendrin (33) and CFTR (26). These results show that maturation ameloblasts express all three Slc26a isoforms in the same membrane domain as CFTR (i.e., the apical plasma membrane, facing forming enamel; Fig. 5). This distribution pattern resembled that in pancreatic tubular epithelium, cells that secrete large amounts of bicarbonates to neutralize acid gastric juice (62). Absence of Slc26a or Dra did not affect enamel structure or mineral density indicating that each of these exchangers expressed alone is not critical for enamel formation. Loss of Slc26a6 resulted in enhanced levels of Dra and Pendrin protein suggesting that ameloblasts compensate the loss of Slc26a by producing more Dra and Pendrin. In pancreatic ductal epithelium the stoichiometry of $Cl^-/HCO3^-$ exchange differs for the various Slc26A isoforms: for pendrin the stoichiometry for Cl-: HCO3- is 1:1 (electroneutral), for Slc26A6 1:2 and for Dra 2:1 (61, 62). In native pancreatic mouse ducts null mutation of apical *Slc26a6* blocked the secretion of bicarbonate and upregulated transport activity across the apical membranes of an exchanger mediating 2:1 exchange, most probably Dra (72). If the same stoichiometry for Cl^-/bicarbonate exchange holds for ameloblast as for pancreatic tubular epithelium similar changes may occur in ameloblasts (Fig. 5.). Slc26a6 would secrete two bicarbonates in exchange for one Cl^-, overall one more negative charge than it imports. This would result into intracellular alkalinization and affect the membrane potential which is compensated by higher Dra and Pendrin activity.

The absence of Dra in ameloblasts on the other hand may result into an increase of the intracellular steady state intracellular pH (as in intestine, (70); but perhaps different in pancreas) which is counteracted by lowering Slc26a6 protein to reduce the driving force for bicarbonate secretion. Functional studies measuring pH and transport of Cl^- are required to test secretion of these ions across the ameloblast layer.

With respect to the small changes in protein levels of Slc26a isotypes in null mutation of *Dra* or *Slc26a*: in pancreatic and salivary ductal epithelium and HEK 293 cells CFTR plays a role by either transducing bicarbonate by itself (Fig.5.) or by stimulating transport activity of DRA, SLC26A6 and PENDRIN as much as 5- to 6-fold without changing the protein levels of these exchangers(61) . Even small changes in protein levels of Slc26a isoforms in mouse ameloblasts could strongly enhance their transport activity to compensate loss of Slc26a6. The absence of a dental phenotype in $Dra^{-/-}$, $Slc26a6^{-/-}$ and $Pendrin^{-/-}$ mice could also be due to compensation by other Slc26a members (Slc 26a7, 26a9

or 26a11) all capable of exchanging bicarbonate and Cl^- Mouse embryos with a double knockout for both Dra and Slc26a6 are not viable and die intrauterine (unpublished results by Dr. U.S). Further studies are needed using tissue-specific or inducible-inactivation of combinations of various Slc26a isoforms to disclose their function in ameloblasts.

In conclusion: The individual inactivation of the Slc26a isoforms does not induce structural changes or mineralization defects in forming enamel. Upregulation of Dra and Slc26a6 protein in Slc26a6-deficient ameloblasts suggests that Slc26a members can compensate for each other.

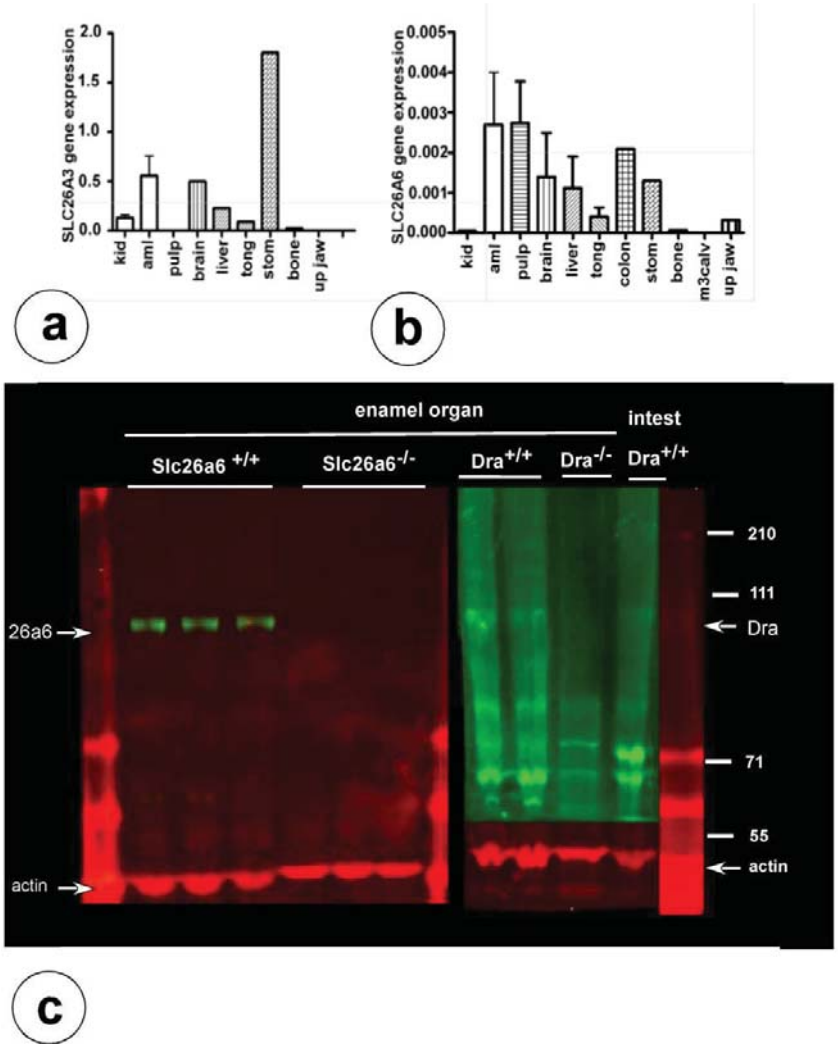

Fig 1. Gene and protein expression for Dra and Slc26a6 in mouse enamel organs. Real-time polymerase chain reaction of mouse wild-type tissues for Dra (a) and Slc26a6 (b) transcripts. The values on the y-axis represent fold difference for the relative mRNA expression (normalized by the housekeeping protein ywhaz; in various tissues. Aml, enamel organ; kid, kidney; m3calv, MC3T3 mouse calvarial osteoblast-like cells; stom, stomach. (c) Western blots of enamel organ extracts from wildtype/Dra$^{+/+}$ and *Dra*$^{-/-}$ mice stained with anti-Dra (right arrow) and *Slc26a6*$^{-/-}$ mice stained with anti-Slc26a6 (left arrow). The 43-kDa bands are positive with anti-actin.

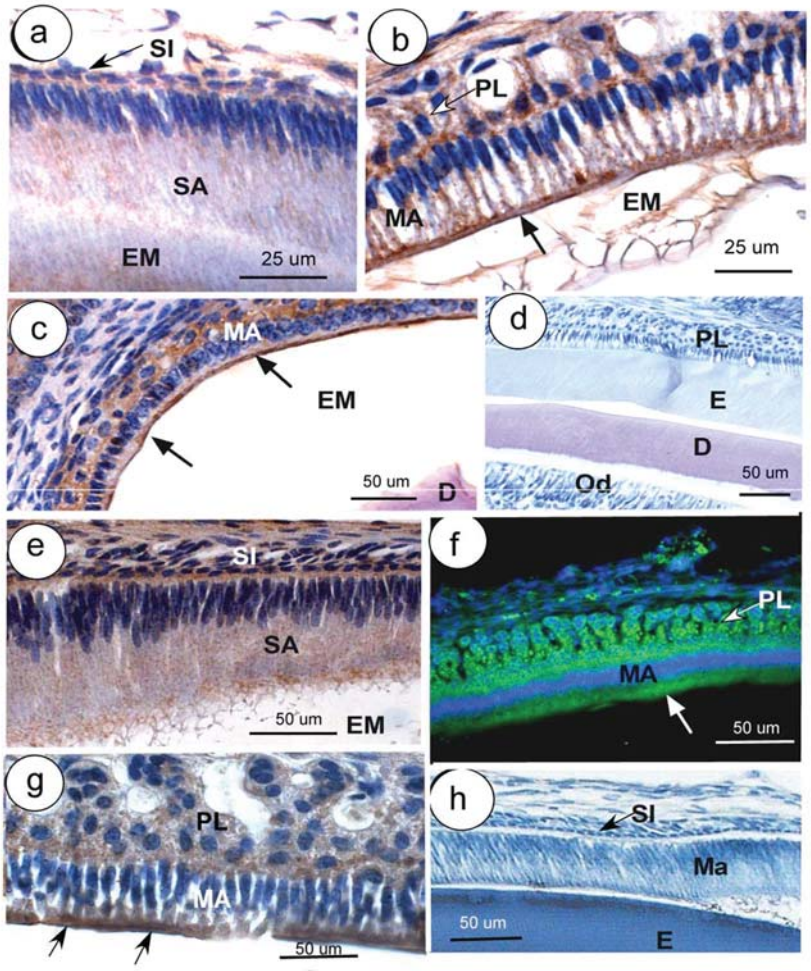

Fig 2. Immunolocalization of Dra (a–d) and Slc26a6 (e–g) in developing mouse teeth. Secretory ameloblasts (SA; a) and maturation ameloblasts (MA; b, c) are positive for Dra, particularly the apical parts (arrows; b, c); some staining is also presents in papillary layer (PL; b, c). (d) A *Dra*$^{-/-}$ incisor stained with anti-Dra. (e) Weak staining for Slc26a6 is seen in late SA, strong staining in MA and PL (f, g). (f, g) Arrows indicate apical staining. (h) Part of an incisor of a wild-type mouse in which anti-Slc26a6 was replaced by nonimmune IgG. Except for panel c (developing molar), all sections were taken from incisors. (f) Immunofluorescent staining (green); all other figures, peroxidase staining (brown). D, dentin; E, enamel; EM, enamel matrix; ES, enamel space; Od, odontoblasts; SI, stratum intermedium (arrows in panels a and h); ST, stratum intermedium.

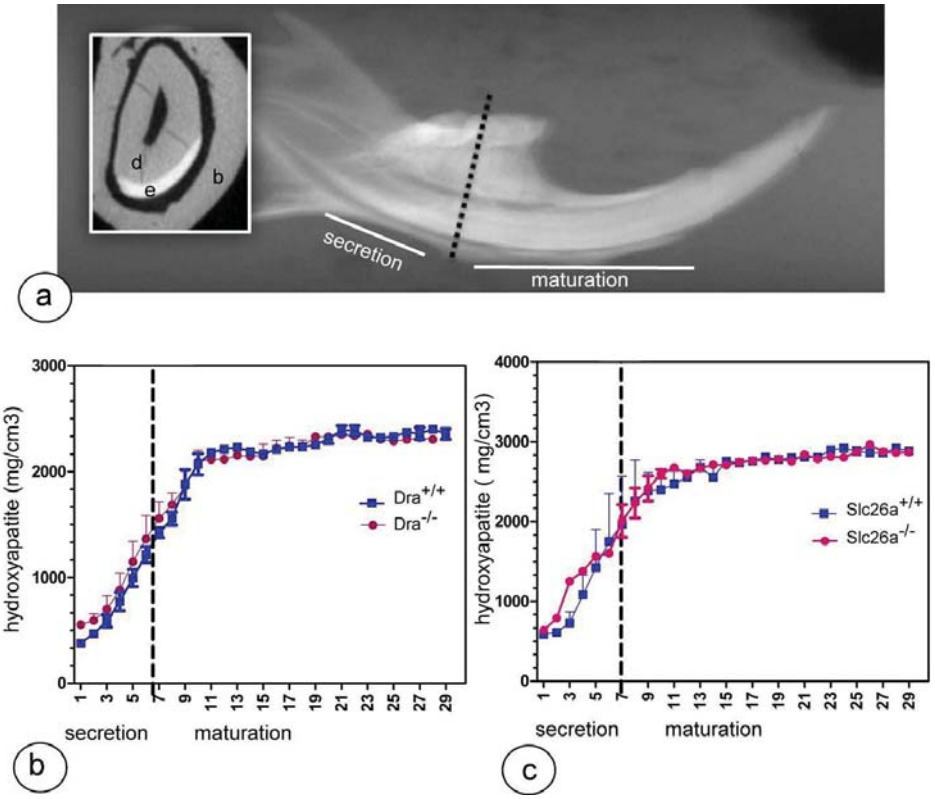

Fig 3. The mineral density of lower incisor enamel. (a) Broken line indicates the reference line between first and second molars indicating the approximate transition from secretory stage to maturation stage (inset: cross section; b, bone; d, dentin; e, enamel) from a wild-type mouse. (b, c) *Dra*$^{-/-}$ and *Slc26a6*$^{-/-}$ mutant mice show mineral density measurements plotted against slice numbers (representing progressive stages of enamel formation with 500-μm intervals). The mineral content of both null mutant mice (red) is not different from that of wild-type littermate controls (blue).

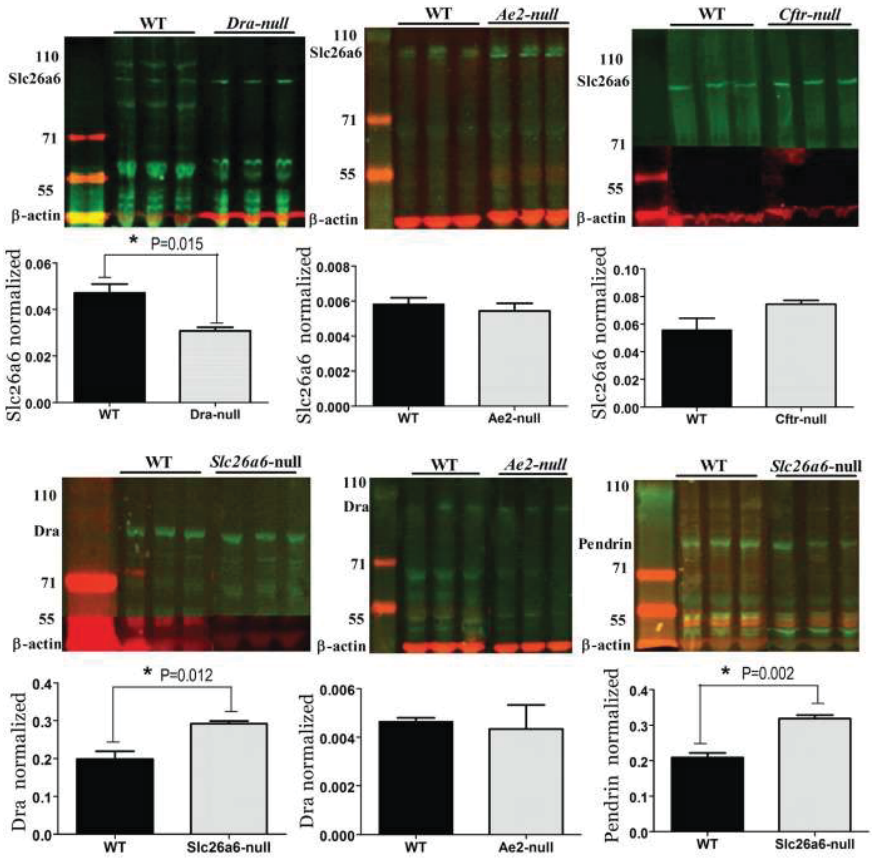

Western blot probed with	Enamel organ Genotype			
	***Slc26a6*-null**	***Dra*-null**	***Ae2*-null**	***Cftr*-null**
Anti-SLC26A6	Negative	-36%*	No change	No change
Anti-DRA	+52%*	Negative	No change	-
Anti-PENDRIN	+55%*	-	-	-

Fig 4. Western blots of enamel organ extracts from *Slc26a*$^{-/-}$ mice stained with anti-Dra, anti-Slc26a6, or anti-Pendrin to detect up- or downregulation of isoforms of the Slc26a family. Top row from left to right: enamel organ extracts from *Dra*$^{-/-}$, *Ae2*$^{-/-}$, and *CFTR*$^{-/-}$ mice stained with anti-Slc26a6. The bar graphs in the second row represent the density measurements. Third row: extracts from *Slc26a6*$^{-/-}$, *Ae2*$^{-/-}$, and *Slc26a6*$^{-/-}$ mice stained with anti-Dra (Slc26a6 and Ae2) or anti-Pendrin. Fourth row represents density measurements. The table at the bottom presents a summary of the changes. WT, wild-type.

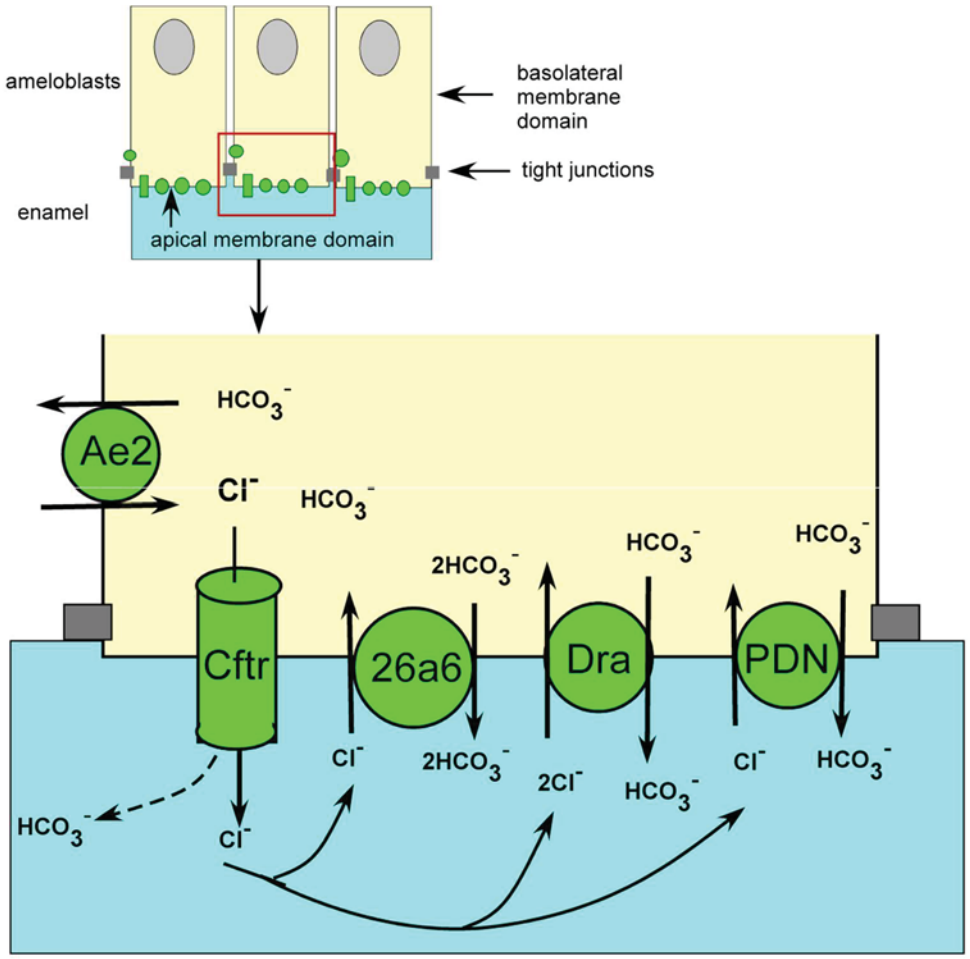

Fig 5. Potential role of Slc26a isotypes during maturation-stage amelogenesis. To neutralize protons released during apatite formation in the enamel space (light blue), the members of Slc26a family secrete bicarbonates in exchange for Cl^-. Basolateral anion exchanger 2 (Ae2) imports Cl^- from the extracellular tissue fluid in exchange for bicarbonate. Cl^- is conducted through CFTR into the enamel, from which it is exchanged back against bicarbonate by Slc26a isotypes. Null mutation of *Slc26a6* is compensated by upregulation of Pendrin and Dra, which requires more Cl^- to transport bicarbonate. Null mutation of *Dra* may change the membrane potential, leading to a drop in activity and in the amount of Slc26a6 protein. CFTR can also conduce bicarbonate up to 25% of its capacity, and can transduce bicarbonate up to 100% of its capacity (36).

Chapter 4

The role of Na^+:K^+:$2Cl^-$ Cotransporter 1(NKCC1/SLC12A2) in dental epithelium during enamel formation in mice

Jalali R, Lodder JC, Zandieh-Doulabi B, Micha D, Melvin JE, Catalan MA, Mansvelder HD, DenBesten P, Bronckers ALJJ. The role of Na:K:2Cl Cotransporter 1 (NKCC1/SLC12A2) in dental epithelium during enamel formation in mice. Front Physiol. DOI: 10.3389/fphys.2017.00709.

ABSTRACT

Na^+:K^+:2Cl^- cotransporters (NKCCs) belong to the SLC12A family of cation-coupled Cl^- transporters. We investigated whether enamel-producing mouse ameloblasts express NKCCs. Transcripts for Nkcc1 were identified in the mouse dental epithelium by RT-qPCR and NKCC1 protein was immunolocalized in outer enamel epithelium and in the papillary layer but not the ameloblast layer. In incisors of *Nkcc1*$^{-/-}$ mice late maturation ameloblasts were disorganized, shorter and the mineral density of the enamel was reduced by 10% compared to wild-type controls. Protein levels of gap junction protein connexin 43, Na^+-dependent bicarbonate cotransporter e1 (NBCe1), and the Cl^--dependent bicarbonate exchangers SLC26A3 and SLC26A6 were upregulated in *Nkcc1*$^{-/-}$ enamel organs while the level of NCKX4/SLC24A4, the major K^+, Na^+ dependent Ca^{2+} transporter in maturation ameloblasts, was slightly downregulated. Whole-cell voltage clamp studies on rat ameloblast-like HAT-7 cells indicated that bumetanide increased ion-channel activity conducting outward currents. Bumetanide also reduced cell volume of HAT-7 cells. We concluded that non-ameloblast dental epithelium expresses NKCC1 to regulate cell volume in enamel organ and provide ameloblasts with Na^+, K^+ and Cl^- ions required for the transport of mineral- and bicarbonate-ions into enamel. Absence of functional NKCC1 likely is compensated by other types of ion- channels and ion transporters. The increased amount of Cx43 in enamel organ cells in *Nkcc1*$^{-/-}$ mice suggests that these cells display a higher number of gap junctions to increase intercellular communication.

INTRODUCTION

Ion transport by ameloblasts is critical for the formation of fully mineralized dental enamel. Disturbance in transport of mineral and/or bicarbonate ions (either local and/or systemic) during enamel development can lead to permanent enamel abnormalities(21, 37).

To form and mature apatite crystals, maturation ameloblasts transport mineral ions as calcium and phosphate into the forming enamel using apical plasma membrane transporter(s) such as Na^+-Ca2$^+$exchangers (NXC1,3) (Okumura et al., 2010) and Na^+-K^+-Ca^{2+} exchangers (NCKX4/SLC24A family) (18, 21, 32). However, formation of each unit cell of the hydroxyapatite crystal also releases approximately 8 protons (73) that need to be buffered to prevent acidification and arrest of mineral accretion. In order to buffer protons, ameloblasts have been proposed to secrete bicarbonate ions into the enamel space that neutralize H^+ (2). Bicarbonate is taken up by ameloblasts basolaterally from the extracellular fluid by bicarbonate-transporting proteins such as electrogenic (NBCe) and electroneutral (NBCn) Na^+-dependent bicarbonate cotransporters expressed in the ameloblasts during secretion- and maturation phase of amelogenesis (21, 55, 74). During maturation phase ameloblasts also generate bicarbonates by producing carbonic acid (H2CO3) from CO2 and H2O via cytosolic carbonic anhydrase 2 (Car2)(74). During the maturation phase the bicarbonate ions are secreted by ameloblasts into the enamel space by coordinated activity of basolateral AE2, and apically by CFTR and members of the SLC26A family: SLC26A1, SLC26A3/Dra, SLC26A4/Pendrin, SLC26A6/Pat1 and SLC26A7(15, 18, 25, 33, 37, 75).
Recent studies suggested that non-ameloblast epithelial cells connected to the basal side of the ameloblasts are also involved in transepithelial transport, based on the expression of NBCe1(14, 37, 55) and Na^+-K^+-ATPase and ATPase activity in papillary layer (14, 52, 76). Accumulation of Na^+ and K^+ and reduction of Cl^- in hypomineralizing enamel of *CFTR*$^{-/-}$ and *Ae2*$^{-/-}$ mice suggested that in wild-type mice Na^+ and K^+ are removed but that Cl^- is taken up from the forming maturation enamel(18). It was speculated that maturation ameloblasts remove Na^+ and K^+ from the enamel space by a yet unknown mechanism which is impaired in *CFTR*$^{-/-}$ and *Ae2*$^{-/-}$ mice. Potential transporters for potassium and sodium reabsorption in ameloblasts may correspond to Na^+:K^+:2Cl^- (NKCC) cotransporters, which are sensitive to loop diuretics such as bumetanide and furosemide (77).

Na^+-K^+-Cl^- cotransporters (NKCCs) aid in the active transport of sodium, potassium and chloride in or out of the cells (78). The SLC12A family contains two Na^+:K^+:2Cl^- cotransporters, NKCC1 and NKCC2, encoded by two different genes (SLC12A2 and SLC12A1, respectively). NKCC1 is widely distributed throughout the body. In salivary glands, basolateral NKCC1 mediates the transport of sodium, potassium and chloride from blood into the acinar cells. Lack of functional NKCC1 results in dramatic reduction of the volume of secreted saliva (79). NKCC1 is also necessary for establishing the potassium-rich

endolymph that bathes part of the cochlea, the organ necessary for hearing. Inhibition of NKCC1, as with furosemide or bumetamide, can result in deafness (80). NKCC2 has a more restricted distribution and is specifically found in the apical membrane of cells in the thick ascending limb of the loop of Henle and the macula densa in nephrons where it serves both in sodium absorption and tubuloglomerular feedback (81). Expression of Slc12a2/Nkcc1 messenger RNA was reported in mouse enamel epithelium in bud to bell stage teeth (embryonic stage E15 –postnatal day 3), suggesting a possible involvement of NKCC1 in enamel organ development (82).

In this study, we tested the hypothesis that NKCC1 plays a role in the ion transport by dental epithelium during enamel formation. The enamel organs of mice and HAT-7 cells, a rat ameloblast-like cell line derived from the cervical loop of a rat incisor (61), were analyzed for expression of NKCC1 at the protein level. The effect of the null mutation of *Nkcc1* on enamel development, cell-size and enamel mineralization was studied by histology, immunohistochemistry, micro-computed tomography (micro-CT) and Western blotting. To understand the role of NKCC1 cell volume regulation, we exposed in vitro HAT-7 cells to bumetanide and measured cell volume using the calcein-quenching method. The effect of bumetamide was also tested on electrophysiology of HAT-7 membranes by patch clamp.

MATERIAL AND METHODS

Tissues

Nkcc1$^{-/-}$ mice used for this study were generated and genotyped as previously described (83). One hemi-maxillary incisor of each mouse was used for immunohistological studies and the other one was freeze-dried for micro-CT analysis and western blotting. For each genotypic mouse strain, at least 3 wild-type mice and 3 null mutant mice were analyzed.

All experiments were approved by the Committee for Animal Care (Vrije Universiteit Amsterdam; ACTA-12-01) and by the Animal Care and Use Committee of the National Institute of Dental and Craniofacial Research, National Institutes of Health (ASP 13–686). The methods were carried out in accordance with the approved guidelines.

Cell culture

HAT-7 cells were grown in DMEM/F12 (Sigma-Aldrich, St. Louis, MO, USA) with 10% HyClone fetal bovine serum, 100 U/mL of penicillin, 10 μg/mL of streptomycin (Sigma-Aldrich) and 10^{-5} mM dexamethasone in humidified atmosphere containing 5% CO2 at 37 °C (74).

Histology

Mouse jaws were fixed by immersion in 5% paraformaldehyde in 0.1 M phosphate buffer pH 7.3 and embedded in paraffin. Calcified tissues from mice older than two weeks were first decalcified in 4% EDTA, pH 7.3 for 2-3 weeks at 4 °C. Salivary glands were fixed in Bouin's fixative (75 ml of saturated picric acid, 25 ml of 40% formaldehyde, and 5 ml of glacial acetic acid) at room temperature for 48 h and processed into 5-7 µm thick paraffin sections. Dewaxed sections were stained with 1% hematoxylin (1 min) and eosin (5 min) (HE) or used for immune-histochemical staining.

Quantifications in cells of the enamel organ

At 40x objective pictures of secretory and maturation stage of enamel organ were made and images selected based on the anatomical position in the tooth. The length of the long axis of secretory and maturation ameloblasts was measured in sagittal sections using imaging software (image J).

Real time quantitative Polymerase Chain Reaction (RT-qPCR)

Total RNA was extracted from HAT-7 cells and various fresh mouse tissues using the NucleoSpin RNA/protein kit (Macherey-Nagel, Düren, Germany) according to the manufacturer's instructions. First strand cDNA synthesis was performed in a 20 µl reverse transcription reaction containing 200 ng of total RNA using VILO kit (Invitrogen) according to the manufacturer's instructions. Real-time PCR analysis was performed to analyze expression of *Slc12a2 (Nkcc1)* with the primer sequences (FW:5' GAAGAAAGTACTCCAACCAGAGATG 3'; REV: 5' CTGAAGTAGACAATCCTGTGATA 3'; size: 232 bps) and the housekeeping protein tyrosine 3-monooxygenase (Ywhaz) with sequences (FW:5'GATGAAGCCATTGCTGAACTTG3'; REV:5'CTATTTGTGGGACAGCATGGA3'; size:229 bps) shown by using the LightCycler 480 system based on SYBR Green I dye (Roche Applied Science, Indianapolis, IN, USA). The LightCycler reactions were prepared in 20 µl total volume with 7 µl PCR-H2O, 0.5 µl forward primer (0.2 µM), 0.5 µl reverse primer (0.2 µM), 10µl LightCycler Mastermix (LightCycler 480 SYBR Green I Master; Roche Applied Science, IN, USA), to which 2 µl of 5 times diluted cDNA was added as PCR template. Controls in the real-time RT-PCR reaction included RT reactions without the reverse transcriptase (control for DNA carry over) and RT reactions without template (control for reagent contamination). With the Light Cycler software, the crossing points were assessed based on a standard curve of 5 serial dilutions ranging from 10 ng to 1.6 pg of cDNA. PCR efficiency (E) was automatically calculated using the fit point method (E = 10−1/slope). Gene expression data were used only if the PCR efficiency was within a 1.85-2.0 range. For each gene the amount of measured DNA was

normalized to that of YWHAZ housekeeping gene to calculate relative gene expression. The relative gene expression in different tissues was normalized to kidney levels for each gene in the graphs.

Immunohistochemistry

Dewaxed paraffin sections were rinsed in phosphate buffered saline (PBS) and subjected to antigen retrieval in 10 mM citrate buffer (pH 6.0) either at 60 °C overnight or for 20 min in microwave at 95 °C. Endogenous peroxidase was blocked with a peroxidase block solution (Envision kit, Dakocytomation) for 5 min. Sections were washed 3x in tris-buffered saline (TBS). Non-specific staining was blocked for 30 min with 2% BSA after which sections were incubated overnight at 4°C with primary antibodies. These were (1) goat anti-NKCC1 (Santa Cruz, affinity purified, catalogue number SC-21545), raised against the N-terminal end of human NKCC1. (2) Mouse anti-NCKX4 monoclonal antibodies (IgG2b isotype) from NeuroMab (UC Davis/NIH NeuroMab Facility, catalogue # N414/25). (3) Matched non-immune IgG (1:200 to 1:300) or normal serum (same concentration as primary antibodies) served as controls. After overnight incubation at 4 °C with primary antibodies, sections were washed 3 times in TBS and incubated with rabbit anti-goat secondary antibody (Thermo Scientific) for 1h at room temperature. After washing staining was visualized using DAB (EnVision kit), counterstained with hematoxylin. For immunofluorescent staining, goat anti mouse–IgG conjugated to Alexa Fluor 488 (5 µg/mL; Invitrogen) was used that counterstained with propidium iodine (Vector Laboratories, Burlingame, CA, USA). Immunohistochemistry images were acquired with a Leica EL6000 or Axio Zoom V16 microscope.

Microcomputed tomography (micro-CT)

To determine the degree of mineral content, hemi-maxillae were scanned at a resolution of 8 µm voxels in a microCT-40 high-resolution scanner (Scanco Medical, AG, Bassersdorf, Switzerland) to measure mineral density in enamel. An internal standard made of solid-sintered apatite (5-mm diameter, 1.5 to 2.0 mm thick, solid sintered) with density of 2.9 ± 0.2 g/mL (a gift from Himed; http://www.himed.com) was used as high-density standard. Beginning at the apical part of the incisor and moving toward the tip, cross-sectioned images through the incisors were collected at sequential intervals of 300 µm in maturation-stage and 60 µm in secretory-stage enamel. In each slice, the mineral density of enamel was measured halfway through the enamel layer at 3 sites within a circular area, with a diameter of 7 µm at the mesial, lateral, and central sides. Mean values and standard error of mean (SEM) of the mineral density were calculated and presented as mean ±SEM. Independent Student's t-test was used to compare the groups. Statistical significance was set at $p < 0.05$ level.

Western blotting

From freeze-dried upper incisors obtained from wild-type and *Nkcc1*$^{-/-}$ mice early maturation stage enamel organs were micro dissected incisally from the location where a reference line projected between lower M1 and M2 intersected the enamel organ of the incisor. The apical half of the enamel organ was dissected, dissolved in non-reducing condition in SDS loading buffer (from Nucleospin Triprep kit, Macherey-Nagel, supplied by Bioke, Leiden, NL) and protein was measured using the BCA protein assay (Bio-Rad, Hercules, CA). Twenty μg of enamel organ denatured protein and 10 μg of molecular weight markers [Novex® Sharp Pre-stained Protein Standard (# LC5800) or SeeBlue® Plus2 Pre-stained Protein Standard (#LC5925)] were subjected to electrophoresis in a 3-8% Tris acetate Nupage gel with Tris acetate running buffer for 60 min at 150 V or 4-12% Bis-Tris Protein Gels with MOPS buffer for 35 min at 200 V. and subsequently electroblotted by an iBlot device (Invitrogen) on nitrocellulose membrane according to the manufacturer's instructions. Membranes were blocked with BSA 2% for 1hour at room temperature and incubated overnight (4oC) with the primary antibodies. Blots were washed 3 times in PBS and incubated with IRDye secondary antibodies (LI-COR). Visualization and quantification was carried out with the LI-COR Odyssey scanner and software (LI-COR Biosciences). Actin was detected at 680 nm wavelength (shown as red) and other primary antibodies and tubulin were detected at 800 nm wavelength (shown as green). Quantification was performed using Odyssey software. Intensity values of the bands were normalized for actin or tubulin and expressed as percentage of wild-type (100%). For western blots the following primary antibodies were used: rabbit anti-SLC26A3/Dra (Research Genetics, Huntsville, AL, USA) , rabbit anti-SLC26A6/Pat1 (donated by Dr. P. Aronson, Yale University, New Haven, CT, USA) (55), rabbit anti-NBCe1 (55) (donated by Dr. W.F. Boron, Case Western Reserve University, Cleveland, Ohio, USA), rabbit anti-NCKX4 (NeuroMab, UC Davis/NIH, # N414/25), rabbit anti-connexin (Abcam, #ab11370), mouse anti-β-actin antibody (Sigma, A2228) and rabbit anti-tubulin antibody (Abcam, ab59680). Secondary antibodies: IRDye 800CW conjugated goat anti-rabbit IgG (H+L) highly cross-adsorbed (LI-COR; Product number: 926-32211) and IRDye 680CW conjugated goat anti-mouse IgG (H+L) highly-cross adsorbed (LI-COR; Product number: 926-32220). Dilutions: anti-β-actin and anti-tubulin (1:1000); other primary antibodies (1:250); secondary antibodies (1:10000).

Imaging of volume decrease after exposure to bumetanide

HAT-7 cells were loaded with 5 μM Calcein-AM (Molecular Probes) for 20 min at 37°C. Changes in cell volume of single HAT-7 cells, plated on poly-lysine coated glass cover slips, were assessed by measuring calcein fluorescence using the calcein-quenching method (84). Cells were bathed in iso-osmotic solution (20-22 °C) and transferred to a continuously

perfused (5ml/min) recording chamber, equipped with a microscope with 10X objective. An image was taken every 30 s. At the start images were obtained for 5 min in the iso-osmotic solution to establish the baseline. Cells were exposed to media supplemented with 10 μM bumetanide for 30 min, after which the iso-osmotic solution was re-introduced and images were taken for another 10 min. The cell surface or average fluorescence of each cell in the acquired images was calculated using Image-J software. Changes in cell surface and average fluorescence were expressed as St/S0 and Ft/F0 ratios, respectively, where S0 and F0 are the average cell surface area and fluorescence under iso-osmotic treatment at the beginning of the experiment.

Electrophysiological recordings

Cover slips bearing HAT-7 cells were transferred to the recording chamber, containing 1.5 ml external solution. The external solution was changed at a rate of 1.5 ml/min using a gravity driven constant perfusion system. During the recordings, HAT-7 cells were perfused with standard artificial Cerebral Spinal Fluid (aCSF) containing (in mM): 126 NaCl, 3KCl, 10 D-glucose, 26 NaHCO3, 1.2 NaH2PO4, 2 CaCl2 and 1 MgSO4, carboxygenated with 95% O2 and 5% CO2 to obtain pH 7.4 and an osmolality of 300 mOsm. For electrophysiological recordings, we used a EPC-8 amplifier and a Instrutech ICT-18 (all from Heka, D-67466 Lambrecht, Germany). Cells were identified and patched using an Olympus IX51 inverted microscope equipped with a LCAcn 40x 0.55nA ph2 objective (all Olympus corporation, Tokyo, Japan). Glass pipettes for whole-cell and cell attached recordings were made from borosilicate capillaries (OD 1.5 mm, ID 0.86 mm; Harvard Apparatus, Holliston, MA, USA) using a Sutter P-87 micro-electrode puller (Sutter instruments, USA) and displayed a resistance of 2.5-5 MΩ. Glass microelectrodes were filled with intracellular solution containing (in mM): 110 K-Gluconate, 10 KCl, 10 HEPES, 0.4 NaGTP, 4 Mg2ATP and 10 K-Phosphocreatine (pH 7.3 adjusted with KOH, 290 mOsm). HAT-7 cells were gently lifted from the cover slip and placed in front of a piezo-driven theta-barrel electrode (TGC 200; Harvard Apparatus, Holliston, MA, USA), filled with standard aCSF on one side and standard aCSF supplemented with 10 μM bumetanide (B1158000 Sigma-Aldrich) on the other side. By changing the position of the barrel bumetanide was applied during the whole-cell recording. Voltage ramps from -70 mV to 80 mV (500ms) were applied under control and in the presence of 10 μM bumetanide.

The cell attached recordings were made by filling the recording pipet with aCSF for the control recordings and with aCSF supplemented 10 μM bumetanide for experimental recordings. All data was acquired using an internal 7-pole Bessel filter (5kHz) and a sample frequency of 20 kHz. Recordings with an access resistance above 12 mΩ were excluded form analysis.

RESULTS

Slc12a2 mRNA expression in mouse tissues and rat HAT-7 cells

Transcripts for *Nkcc1/Slc12a2* normalized for *Ywhaz* housekeeping gene for were detectable in kidney, enamel organs, intestine and pulp; in the remaining tissues tested expression was very low or below detection limit (Fig 1a). HAT-7 cells also expressed *Nkcc1* transcripts (Fig 1b).

Bumetanide blocks activity of the NKCC's. To test whether this blocking agent also could affect *Nkcc1* expression level in enamel epithelium, HAT-7 cells were exposed to various concentrations of this inhibitor for 45 min, washed, and incubated for 9 h in medium without inhibitor. Then total RNA was isolated and the amount of Nkcc1 transcripts measured by RT-qPCR (Fig. 1b). Bumetanide did not change the number of transcripts of Nkcc1.

NKCC1 expression in HAT-7 cells, mouse enamel organ and salivary glands

Anti-NKCC1 antibodies stained plasma membranes in HAT-7 cells as fine granular material (Fig. 2a). Replacing primary (mouse) antibodies for normal non-immune mouse IgG failed to stain these membranes in HAT-7 cells (Fig. 2b).

Strong immunostaining was detected in the basolateral plasma membranes of the acinar cells of salivary glands, a well-established site of NKCC1 expression (Evans et al., 2000) (Fig. 2c).

In upper incisors, in presecretory stage and during the secretory and maturation stage, the plasma membrane of outer enamel epithelium cells was immunopositive for NKCC1 (Fig. 2e,f). No staining was seen in ameloblasts. Weaker staining was seen in dental epithelium between ameloblasts and outer enamel epithelium. Strong staining was apparent in the papillary layer (intracellular and membranes) during maturation (Fig. 2e,g).

Sections from salivary glands (Fig. 2d) and enamel organ from *Nkcc1*$^{-/-}$ mice (Fig. 2h) incubated with anti-NKCC1 failed to immunostain the tissues, validating the specificity of the antibodies.

NKCC1 expression is important for enamel organ function and enamel mineralization

*Slc12a2 (*or *Nkcc1)* knockout mice exhibit growth retardation with a 30% incidence of death by the time of weaning. They are deaf, have less body fat, reduced mean arterial blood pressure, exhibit reduced cAMP-induced short circuit currents in jejunum, cecum, and trachea, unusual head postures, and engage in circling behaviors and rapid spinning, but have difficulty maintaining their balance (83). Incisors of *Nkcc1*$^{-/-}$ mice showed no obvious gross

changes. Analysis of upper incisor enamel of *Nkcc1*$^{-/-}$ mice showed no significant change in mineral density in enamel during secretory stage but a reduction at maturation stage, reaching a final density that was reduced about 10% compared to controls ($P < 0.0001$) (Fig. 3h and i).

Analysis of histological sections of *Nkcc1*$^{-/-}$ upper mouse incisors showed that late maturation ameloblasts lost their polarization and that the cells of the papillary layer were shorter compared to that seen in wild-type controls. However, secretory stage ameloblasts and stratum intermedium seemed hardly or not affected in the null mutants in comparison to wild-type mice (Fig 5 f, g, i and j).

Next we examined expression of NCKX4 (sodium/calcium-potassium exchanger-4) a major transcellular calcium transporter in maturation ameloblasts, to determine whether calcium transport is affected in *Nkcc1*$^{-/-}$ incisor. Nckx4 protein was strongly expressed in the apical membrane of maturation ameloblasts of wild-type mice (Fig. 3a), but its antibody-associated staining was weaker in *Nkcc1*$^{-/-}$ mice (Fig. 3b). Western blot analysis (Fig. 3c) of protein extracts from wild-type and *Nkcc1*$^{-/-}$ maturation enamel organ, showed a small (but not significant) reduction of NCKX4 protein in *Nkcc1*$^{-/-}$ enamel organ (Fig. 3d)

Upregulation of SLC26A6, DRA, NBCe1 and gap junction (Cx43) protein expression in Nkcc1$^{-/-}$ *enamel organ by Western blotting*

To examine if the expression of other Na^+ and Cl^- ion transporters or/ and gap junction channels could compensate for the absence of NKCC1, we tested maturation stage enamel organs of *Nkcc1*$^{-/-}$ mice for changes in protein levels of SLC26A6, DRA, NBCe1 and Cx43 by Western blotting (Fig. 4 a-h). Total protein extracted from *Nkcc1*$^{-/-}$ enamel organs showed a 303% increase of SLC26A6/PAT1 ($P=0.003$) (Fig. 4a and e) compared with wild-type a, 143% increase for SLC26A3/DRA ($P=0.04$) (Fig. 4b and f), 47% increase for NBCe1 ($P=0.04$) (Fig. 4c and g) and 78% increase for Cx43 ($P=0.01$) (Fig. 4d and h). The results are summarized in Fig. 4i panel.

Regulation of cell volume is impaired in Nkcc1$^{-/-}$ *enamel organ and HAT-7 cells exposed to bumetanide*

NKCC1 is one of the proteins involved in cell volume recovery after cell shrinkage in kidney (85). To examine a possible role of NKCC1 in regulating cell volume in ameloblasts, we measured cell volume changes of single HAT-7 cells in vitro using the calcein-quenching method before and after bumetanide (10 uM) treatment, (Fig. 5 a-e). Bumetanide decreased cell volume as measured directly (Fig. 5d) and by loss of fluorescence (Fig. 5e). In incisors of *Nkcc1*$^{-/-}$ mice the values of the long axes of secretory ameloblasts were not different from

those in wild-types (Fig. 5f, g and h) but were significantly shorter (~ 25%; P<0.0001; Fig. 5i, j,k) in maturation ameloblasts.

Bumetanide increases membrane conductance in HAT-7 cells

Bumetanide has been previously shown to induce potassium currents in canine kidney cells. To test whether bumetanide affects the membrane ionic conductance in HAT-7 cells, electrophysiological whole-cell voltage-clamp recordings were made from these cells. The membrane potential was ramped from -70 mV to +80 mV. In control conditions, the voltage ramp induced a small membrane current that reversed at -30 mV. Application of bumetanide (10 μM) increased membrane currents across the entire membrane potential range (Fig 6a). The outward current measured at +80 mV increased about three fold, whereas the inward current measured at -70 mV was twenty fold enlarged (Fig 6a). The increase of membrane currents induced by bumetanide hardly reversed upon washout (not shown). To our surprise, the bumetanide-induced currents reversed at -30 mV. Given that for the recording solutions used in these experiments the equilibrium potential for potassium was -95 mV, for chloride -65 mV and for sodium and calcium above +60 mV, this suggests that most likely a mixed ionic current was activated by bumetanide-block of NKCC transporters.

Bumetanide increases ion channel activity in HAT-7 cells

It is not known whether the effect of bumetanide on the membrane conductance required block of NKCC transporters across the entire cell membrane, or whether this effect could also be induced locally. To determine this, we made cell-attached recordings from HAT-7 cells and applied bumetanide only to the membrane patch inside the patch pipette. The pipette potential was kept at 0 mV. In control recordings, ion channel activity and occasional discrete single channel openings were observed that were alternated by silent periods (n=10, Fig 7). At this pipette potential, only outward currents were observed. During recordings in which bumetanide (10 uM) was included in the recording pipette, ion channel activity conducting outward currents increased (n=10, Fig.7). No discrete amplitude levels could be distinguished, which suggests that blocking NKCC transporters with bumetanide augments the activity of multiple ion channels in the membrane patch. These results suggest that the effects of bumetanide on membrane ionic conductance could be induced locally in a patch of the cell membrane.

DISCUSSION

The present study demonstrates that in mice enamel organ epithelium in secretory and maturation stage expresses NKCC1 at the mRNA and protein level. Without NKCC1 enamel was slightly less mineralized, at visual inspection without gross change in enamel structure.

The upregulation of NBCe1, DRA and PAT1 in enamel organs of *Nkcc1*$^{-/-}$ mice suggest that NKCC1 can be at least in part compensated by typical pH regulators as reported for salivary glands and duodenum epithelium in *Nkcc1*$^{-/-}$ mice (79, 85). This suggests that NKCC1 is involved in enamel mineralization possibly by providing ameloblasts Cl^- crucial for bicarbonate secretion but its role is limited. However, it cannot be excluded that some of the defects in enamel mineralization are secondary due to systemic changes brought about by other tissues in *Nkcc1*$^{-/-}$ mice.

The reduction in mineral density of enamel in *Nkcc1*$^{-/-}$ mice was relatively small (10%) in comparison with the reduction in *Cftr*$^{-/-}$ mice (47%, (18)) and in *Ae2*$^{-/-}$ mice (45%(25)), two transporters critical for pH regulation by maturation ameloblasts. The reduction in mineral density in *Nkcc1*$^{-/-}$ mice could be due to: (1.) a slightly increased acidification associated with reduced intracellular Cl^- levels in ameloblasts resulting from less NKCC1-mediated Cl^- transport in the papillary layer. The rather normal gross appearance of incisor enamel and the fact the mineral density changes appear quite late in comparison to the severe mineral reduction in enamel of *Cftr*$^{-/-}$ and *Ae2*$^{-/-}$ mice seen early in maturation make this option less likely. (2) Reduction of the cytosolic levels of K^+ or a reduced number of apical NCKX4 in maturation ameloblasts needed for NCKX4-mediated Ca^{2+} transport by maturation ameloblasts. (3). Reduction in the levels of Na+ in ameloblasts required for Na-Pi2b mediated phosphate transport (18).

Ameloblast did not express NKCC1 but papillary layer cells highly expressed the cotransporter. To reach forming enamel ions transported by NKCC1 into the papillary layer pass from papillary layer into ameloblasts. The enhanced expression of connex43 points to a mechanism for such transport. Ameloblasts and papillary layer have been suggested to act as a functional unit in passing ions from outer enamel epithelium to ameloblasts through gap junctions (14). Gap junctions are structures passing through the plasma membranes of two adjacent cells forming small pores that enable direct intracellular transport of ions and small molecules/peptides (17). The significance of communication between enamel organ cells is exemplified in Gja1$^{Jrt-/+}$ mice in which enamel formation was severely affected by a decrease in the number of gap junctions in the enamel organ (17). Upregulation of connexin43 in enamel organ of *Nkcc1*$^{-/-}$ mice may occur to increase the number of gap junctions to compensate for changes in ion transport due to absence of NKCC1.

Our histological and electrophysiological results confirm that NKCC1 is involved in amelogenesis. The distribution of NKCC1 in enamel organs, and the reduction in cell height of ameloblast layer in *Nkcc1*$^{-/-}$ mice suggests that during amelogenesis the symporter NKCC1 serves to import Na^+, K^+ and Cl^- from blood vessels, regulates cell volume of dental epithelium and likely water transport across the ameloblast layer. Transport of large amounts of Cl^- and Na^+ across epithelial cells, for example by Cl^- channels and cotransporters such as

CFTR, NKCC2 and NKCC1, is required for fluid transport (e.g. in kidney) and maintenance or changes in cell volume. Volume changes in ameloblasts during normal amelogenesis are substantial indicated by the changes in the long axes of ameloblasts when moving from differentiation into secretion stage, reaching maximal values at full secretion stage, followed by a 50% reduction during transitional and early maturation stage. In *Nkcc1*$^{-/-}$ mice the maturation ameloblasts were shorter than in wild-type controls. Exposing HAT-7 cells to 10uM bumetanide caused cell volume decrease without altering the number of Nkcc1-mRNA transcripts suggesting that iso-osmotically shrinkage accrued after adding bumetanide. These data are in line with a function of NKCC1 in cell volume regulation and ion transport.

In short, NKCC1 is highly expressed in non-ameloblast enamel organ epithelium. A reduction in mineral density of enamel, shortening of ameloblast cell body and upregulation of other ion transporters when NKCC1 is absent suggests that NKCC1 regulates cell volume and ion transport but can be partly compensated by enhanced activity of other ion transporters.

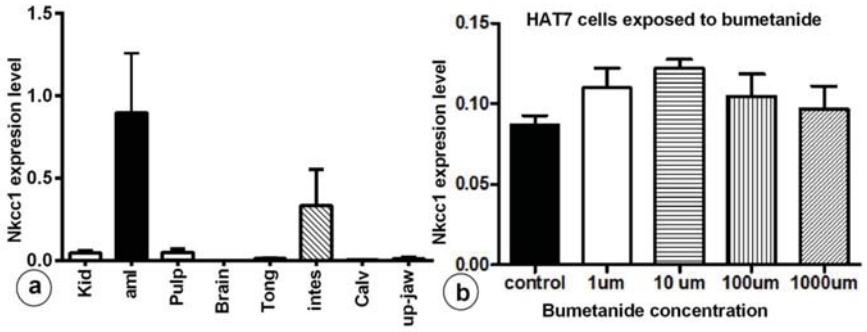

Fig 1. High mRNA expression of Nkcc1 in mouse enamel organ (a) and HAT-7 cells (b) and effect of bumetanide on Nkcc1 expression in HAT-7 cells (b). In fig 1a total RNA was extracted from different tissues and Nkcc1 expression values normalized for ywhaz. Tissues are listed along X-axis (average for n=3 mice). (b) Total RNA was isolated from HAT-7 cells treated with zero (control) and different concentrations of bumetanide (1µm,10µm,100µm,1000µm). kid: kidney; aml: ameloblasts/enamel organ; tong: tongue; intes: intestine; calv: calvaria; up-jaw: upper jaw

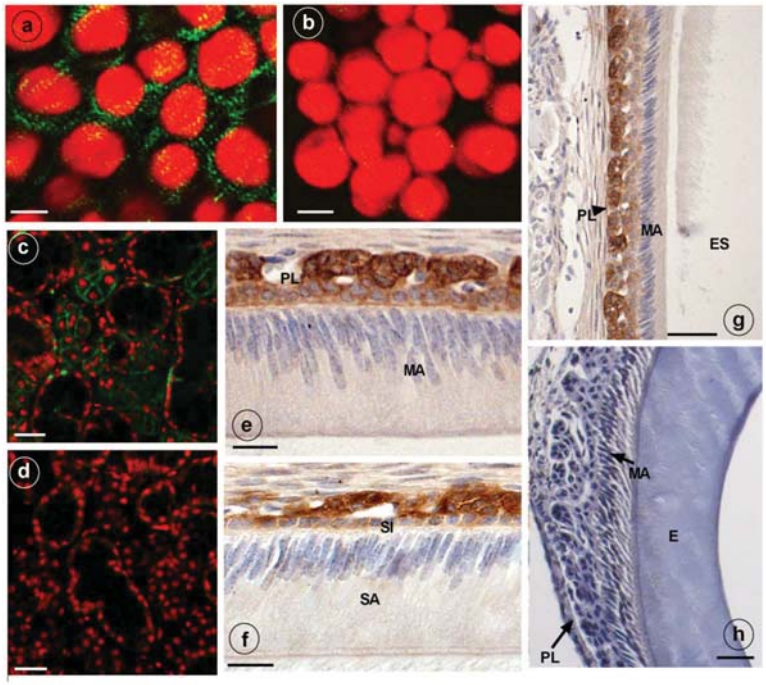

Fig 2. Immunostaining of NKCC1 protein in HAT-7 cells, developing mouse dental epithelium and mouse salivary glands. NKCC1 expression as green punctuate grains near the plasma membranes of cultured HAT-7 cells stained with anti-NKCC1 (a) or with non-immune IgG (b, control) and visualized using Alexa488-coupled secondary antibody. (c and d) show salivary glands of a wild type (c) and *Nkcc1*$^{-/-}$ mouse (g) stained with anti-NKCC1. NKCC1 staining in mouse dental epithelium at secretory stage (f) from OEE till ameloblast layer and in maturation stage (e, g) in papillary layer. Absence of staining with anti-NKCC1 in salivary gland (d) and incisor (h) of a *Nkcc1*$^{-/-}$ mouse confirms the specificity of primary antibody. Note: all the staining have been tested in triplicate in three mice. E, enamel; ES, enamel space; SA, ameloblasts secretory stage; MA, ameloblast maturation stage; P, pulp; PL, papillary layer; SI, stratum intermedium;

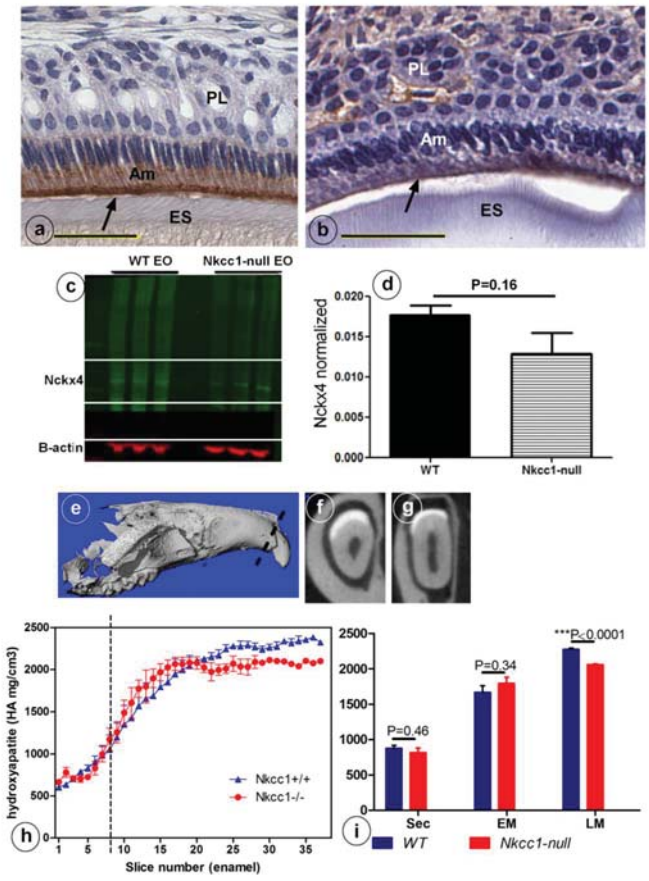

Fig 3. Reduced NCKX4 protein expression in enamel organ and lower mineral density of enamel in maturation stage ameloblasts of *Nkcc1*$^{-/-}$ upper incisors (n=3) (a-d) and decrease in maturation mineral density in mouse upper incisor (n=3). (e-i) shows the importance of NKCC1 for enamel mineralization. Nckx4 expression (arrows) in WT (a) and *Nkcc1*$^{-/-}$ maturation ameloblast (b). Total protein was extracted from WT and *Nkcc1*$^{-/-}$ enamel organs (n=3 mice) and NCKX4 expression analyzed by western blot (c). Graph bar shows semi-quantitative NCKX4 band density normalized to that of ß-actin (d). Mineral density measured by micro-CT plotted against slice numbers (h). Blue color represents WT and red *Nkcc1*$^{-/-}$ upper incisor; maturation stage starts at the dotted line. In (i) the bar graphs with the same color (blue and red) represent measurements of mineral density in different stages of amelogenesis (sec=secretory; EM, early maturation; LM, late maturation). (e,f,g) show 3D reconstruction, virtual cross section of WT and *Nkcc1*$^{-/-}$ upper incisor respectively. Circles in (f) indicate sites of measurement per slice.

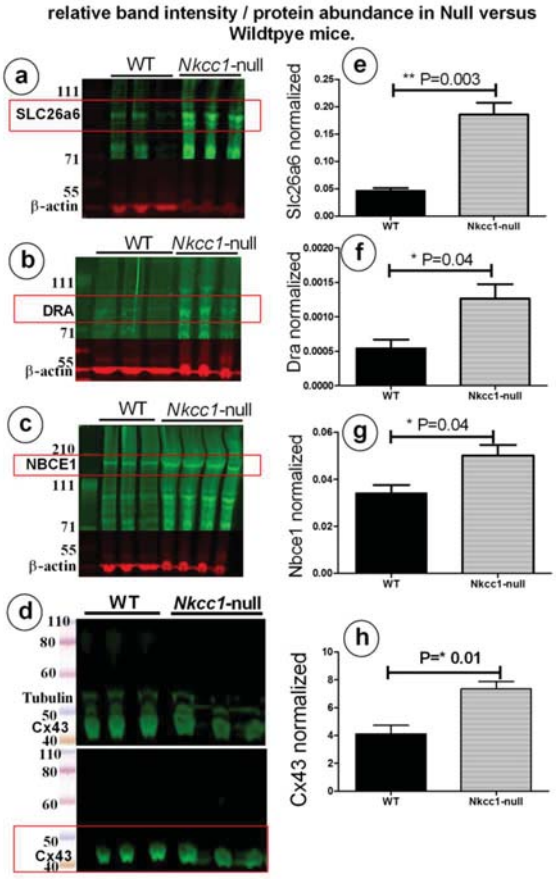

i Enamel Organ	Western blot probed with			
Genotype	Anti-SLC26A6	Anti-DRA	Anti-NBCE1	Anti-CX43
Nkcc1-null	+303 %**	+143.4 %*	+47.4 %*	+78 %*

Fig 4. SLC26a6, DRA, NBCe1 and CX43 proteins possibly compensate during lost Nkcc1 gene expression. Expression of SLC26a6 (a), DRA (b), NBCe1 (c) and Cx43(d) protein extracts of enamel organs of WT and *Nkcc1*$^{-/-}$ mice by western blotting. Graph bars (e,f,g) show semi-quantitative SLC26a6, DRA, NBCe1 bands normalized to ß-actin. The CX43 bands were normalized to tubulin (h). Table (i) presents a summary of the quantification results presented as *Nkcc1*$^{-/-}$/wild-type x100%

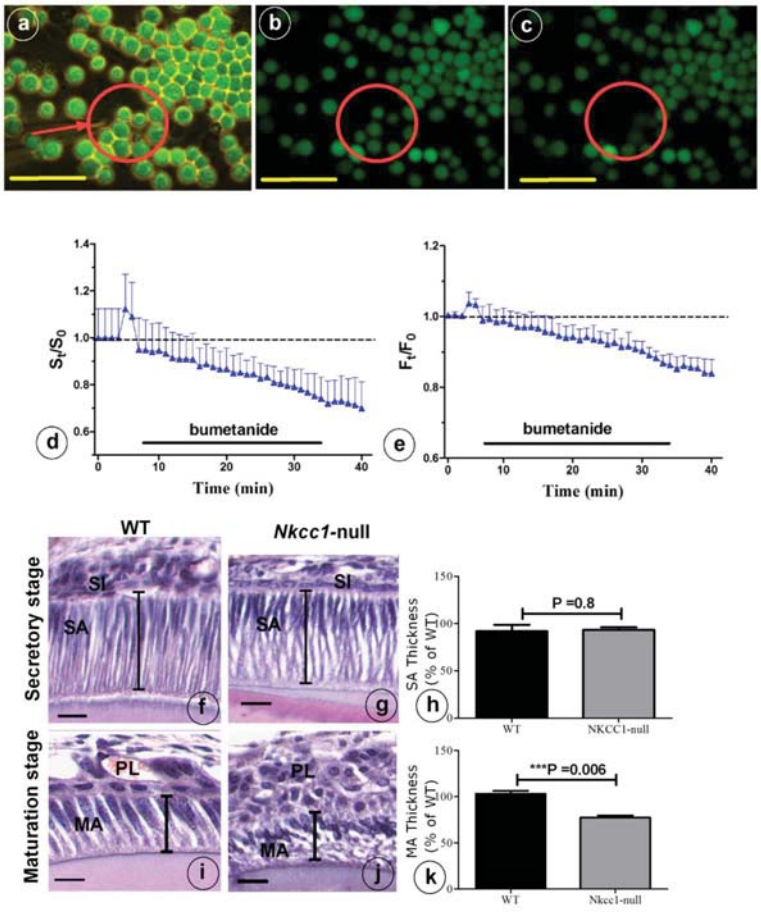

Fig 5. NKCC1-dependent regulatory volume decrease. (a) HAT-7 cells were loaded with 5µM Calcein-AM for 20 min. Cells were bathed in a iso-osmotic solution that was switched to 10µM bumetanide solution for 30 min as indicated by black bars in (d,e). Changes in cell volume of single HAT-7 cells (arrow in a). (b) 2min after bumetanide exposure; (c) 7 min after bumetanide exposure. (d) average relative cell surface and (e) fluorescence, obtained under iso-osmotic with and without 10µM bumetanide (n=10). Length of ameloblast cells in *Nkcc1*$^{-/-}$ (g-j) and WT mice stained with H&E was measured using Image-J software (n=3). Bar diagrams show the difference between ameloblasts length in the secretion stage (h) and maturation stage (k) of amelogenesis in WT and *Nkcc1*$^{-/-}$ mice. SA, secretory ameloblast; MA, advanced maturation ameloblasts; SI, stratum intermedium; PL, papillary layer. Lines indicate length "thickness" of the cells in f, g, i and J; results for f and g summarized in h, while results for Fig.5 i and j are summarized in Fig.5 k. Bars=50µm

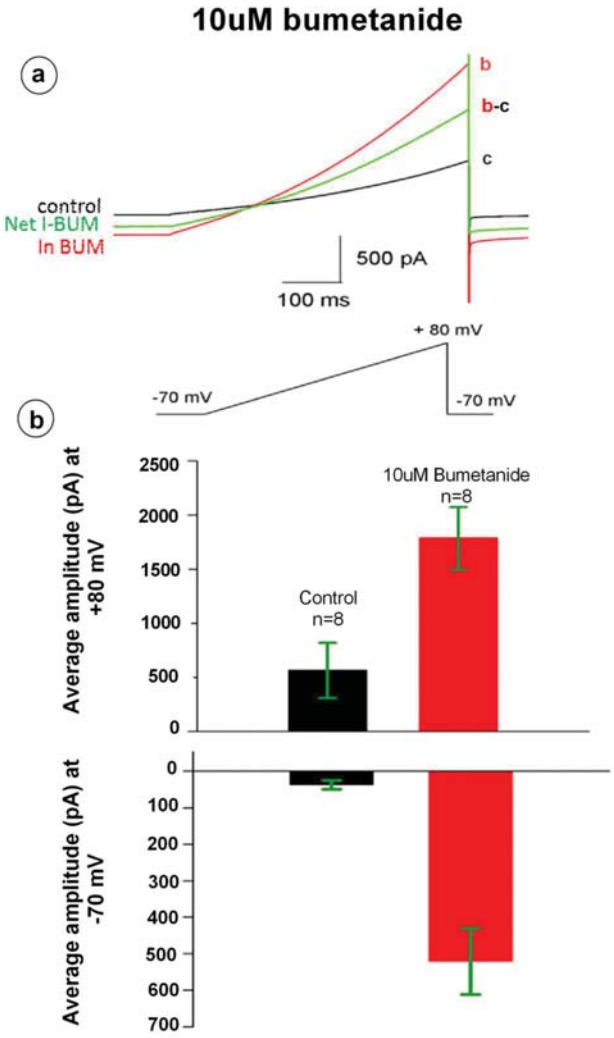

Fig 6. (a) Bumetanide 10 µM increased whole-cell membrane currents across the voltage range from -70 mV to +80 mV. The black tracing (c) is the control and the red ACSF tracing (b) is the current in the presence of 10 µM bumetanide. The green tracing (c-b) is the net current induced by 10 µM bumetanide. (b) outward currents measured at +80 mV (upper b) and inward current at -70 mV (lower b). Bars show the average amplitude of control and 10 µM bumetanide (n= 8)

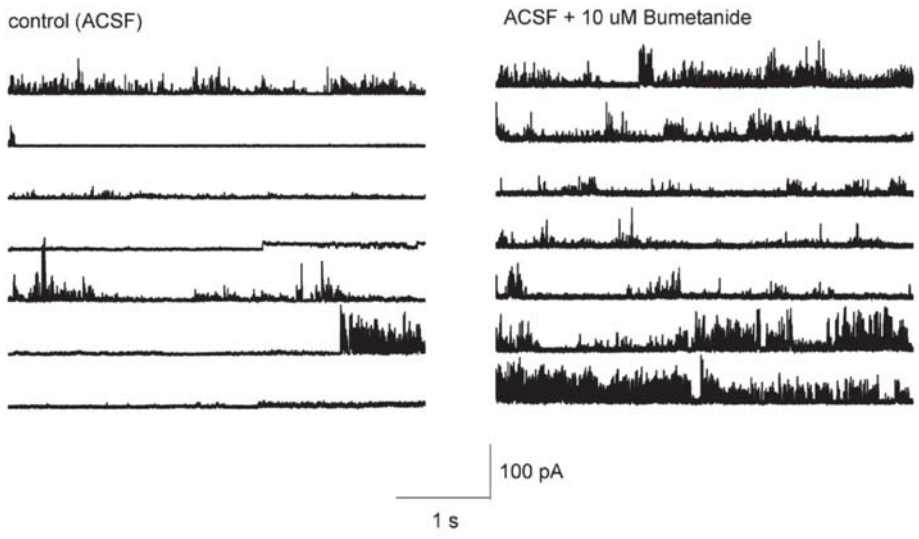

Fig 7. Representative tracings showing the effect of 10 µM bumetanide on the channel activity in HAT-7 cells. Left figure shows the channel activity obtained from cell-attached patch with ACSF in the recording pipet at 0 mV. Right figure shows the channel activity obtained when the recording pipet was filled with aCSF + 10 µM bumetanide and clamped at 0 mV.

Chapter 5

Mineralization defects are comparable in fluorotic impacted human teeth and fluorotic mouse incisors

Jalali R, Guy F, Ghazanfari S, Lyaruu D, van Ruijven L, DenBesten P, Martignon S, Castiblanco G, Bronckers ALJJ. Mineralization-defects are comparable in fluorotic impacted human teeth and fluorotic mouse incisors. Arch Oral Biol. 2017;83:214-221.

ABSTRACT

Fluoride excess of 0.05–0.07 mg F/kg bw/day in water or food additives like salt are the principal cause of endemic dental fluorosis. How fluoride causes these defects is not clear yet. Recent studies in rodent suggests that development of enamel fluorosis is associated with insufficient neutralization of protons released during the formation of hypermineralized lines. Here we examined whether hypermineralization could also be assessed by Micro-CT in developing molar enamel of humans exposed to fluoride. Micro-CT analysis of hypomineralized enamel from human fluorotic molars graded by the Thylstrup-Fejerskov (TF) Index as III-IV showed weak hypermineralized lines and hypermineralized patches not seen in TF-I/II grade enamel. The mesio-distal sides of these molar teeth were significantly smaller (~18%, p= 0.02) than in TF-I/II teeth. The patterns of changes observed in human fluorotic teeth were similar to those in fluorotic rodent incisors. The data are consistent with the hypothesis that also in developing human teeth fluoride-stimulated local acidification of enamel could be a mechanism for developing fluorotic enamel.

INTRODUCTION

Dental fluorosis is the hypomineralization of dental enamel caused by chronic ingestion of fluoride during the formative stages of the dental hard tissue (86). The severity of the condition depends on the time, dose and duration of fluoride intake (86). Clinically, human enamel fluorosis ranges from mild (containing more accentuated perikymata) to more severe fluorosis when the teeth develop white opacities. Most severe changes seen when teeth have erupted are extensive enamel pitting and partial loss of enamel, presumably formed after eruption (87). To investigate the mechanisms of fluorosis many studies(88-91) made use of experimental animals mostly rodents. Important is also that rodents develop enamel fluorosis at the same plasma F levels as in human (31, 92).

Ameloblasts produce tooth enamel in a two-step process. During the secretory stage, ameloblasts secrete an organic matrix mostly consisting of amelogenins. At the end of this stage, the enamel layer achieves its full thickness. Moderate-to-high exposure of rodents to fluoride - especially at the beginning of secretory stage - can influence the ameloblast structure, enamel matrix mineralization and the thickness of the enamel layer (93-96). During secretion stage but most by maturation stage amelogenins are degraded by proteases such as MMP20 (secretion stage) and KLK4 (maturation stage), while enamel continues to mineralize till completion (2). Enamel hypomineralization, seen after exposure of mice or rats to drinking water containing 25ppm fluoride or more suggests that fluoride impairs calcium (31) phosphate crystal growth preeruptively. Isolated and confluent pits seen in severely affected human fluorotic teeth may be post-eruptively by mechanical trauma of hypomineralized surface enamel (87).Several mechanisms have been proposed responsible for formation of fluorotic enamel, e.g. impaired transport of mineral ions, reduced expression of mineral ion transporters (97) or reduced secretion of proteases but not their direct inhibition by fluoride (98). Recently, it was proposed that enamel fluorosis may develop due to generation of extra protons by fluoride-induced acceleration of crystal formation (89) as seen in rodent enamel after a high dose of fluoride or in tooth organ cultures exposed to fluoride in vitro (99). Ameloblasts appear to have the machinery to produce and secrete bicarbonates (33, 37, 74). In mice fluorosis s far more pronounced when pH buffering by ameloblasts is disrupted by null mutation of pH regulators, supporting the relevance of buffering protons during mineralization in enamel in forming enamel (89).

Here we examined whether hypermineralization could also be assessed by Micro-CT in developing molar enamel of humans exposed to fluoride. To avoid post-eruptive changes in enamel, we used in this study impacted teeth. We also examined the enamel of impacted human teeth for the presence of surface irregularities to see if pits and grooves could develop pre-eruptively. Based on reports that long-term exposure of rats to 100 ppm fluoride in drinking water reduced the thickness of enamel (95), we furthermore measured

the thickness of the enamel layer and the crown dimensions in these human and mice fluorotic teeth.

METHODS AND MATERIALS

Human material

Twelve upper third molars were collected from Bogota, Columbia. The severity of dental fluorosis was scored by two dentists according to the Thylstrup-Fejerskov Index (TF) and ranged from low (TF-I/II, n=6) to moderate degree of fluorosis (TF-III/IV; n=6). Since in Bogota no teeth completely free from fluorotic changes could be collected three unerupted 3rd upper molars without any sign of fluorosis were collected at the VU medical center. In the Netherlands drinking water or salt are not fluoridated.

Unerupted upper third molars were collected from donors 16-30 years-old attending the Oral Surgery clinics at the Dental Faculty, Universidad El Bosque in Bogotá, Colombia (an area with high prevalence of fluorosis and 180-220 mg F/kg added to salt since 1989) (100). All subjects used twice/day fluoridated toothpaste (1000-1500 ppm F). Daily average fluoride intake by subjects from Bogotá has been reported as 0.11±0.10 mg F/kg body weight (1.43±1.14 mg F/day) based on an assessment by questionnaire, filled in by subjects with permission of their parents if the subjects were younger than 18 year. It included questions on social– demographical data, oral hygiene habits, fluoride-use habits and the instructions they received for the oral care. Two trained and experienced examiners (SM, GC) visually assessed the teeth with signs of fluorosis using the TF index (87), and agreed in the severity score. From the pool of teeth, 12 were selected from Bogota: TF-I/II (n=6), TF-III/IV (n=6). Since it was not possible to obtain control teeth completely free from any sign of fluorosis in Bogota age-matched-non-fluorotic human third molar control teeth (donors 16-30 years-old) (n=3) were collected at the VU University Medical Center, Amsterdam used as non-fluorotic negative controls. Donors signed a tooth-donation term and the study was approved by the Ethical Board of Universidad El Bosque (UB.267.2010) and VU-Medical Centre, Amsterdam. Teeth were extracted for orthodontic or prophylactic reasons. Immediately after extraction, a pool of molars undamaged by the surgical procedure were rinsed with tap water and put in phosphate-buffered saline with 0.02% thymol (PBS-T). At the lab, soft tissue and blood residues were removed with scalpel and prophylactic brush and stored at 4°C in PBS-T.

Animals

Three-week old mice (C57Bl) were divided into 2 groups and given drinking water containing either 0 or 100 mg of F/L (221 mg/L NaCl) for 6 weeks. After euthanasia of the mice hemimandibles were excised, snap-frozen in liquid nitrogen, freeze-dried, and mounted

in a holder for Micro-CT scanning. All experiments were approved by the Committee for Animal Care (Vrije Universiteit Amsterdam; ACTA-12-01). The methods were carried out in accordance with the approved guidelines. Plasma levels of the mice at time of sacrifice were 10 micromoles/L in fluorotic mice and 2 micromoles/L in controls.

Quantitative light-induced fluorescence (QLF) analysis

In areas of the enamel where hypomineralization was present, a decrease of fluorescence intensity could be seen (Fig. 1d). Photographs of these fluorescent areas were taken from all surfaces of the crowns of the extracted molars using a QLF-D camera (Inspector Research Systems BV, Amsterdam, The Netherlands). It consists of a Canon 450-D SLR camera equipped with an illumination tube and uses an excitation wavelength of 405±20 nm and filtering optics in front of the camera lens. The photographs were taken using dedicated software (C3 v 1.25; Inspektor Research Systems) in a dark room with fixed camera settings (shutter speed 1/160e; aperture value 5.6; ISO1600). The tooth surfaces were washed in deionized water and dried before the photographs were taken. The roots of the molars were placed in a clay block to fix the molars and to standardize the distance between the teeth and the lens of the camera. The photographs were analyzed by a single examiner using Image-J software (Image-J 1.33u software; http://rsb.info.nih.gov/ij/index.html). The fluorotic surface (white spot size) of a tooth was calculated as the affected enamel (dark non-fluorescent area of the crown area in mm^2) divided by the total area of the crown surface (in mm^2) times 100.

Micro-CT

The teeth (human and mice) were scanned with Mirco-CT 40 (Scanco Medical AG, Bruttisellen, Switzerland). This scanner is calibrated weekly using a phantom with densities from 0 to 3000 mg HA/cm^3. Teeth were mounted in a holder and placed in the scanner in such a manner to minimize the FOV (field of view). Voxels near the enamel surface were excluded to preclude Micro-CT partial volume effect. The integration time was set at 300 ms, the beam intensity at 55kV, the current at 145 µA and the resolution set at 18µ for both mice and human teeth. An internal standard made of solid-sintered apatite (5-mm diameter, 1.5 to 2.0 mm thick) with density of 2.9 ± 0.2 g/mL (a gift from Himed; http://www.himed.com) was used as high-density standard. Three-dimensional (3D) reconstructions were made using the cone beam reconstruction algorithm. Using two-dimensional-horizontal cross-sections, mean mineral density was measured at nine circular regions of interest (Fig. 3a). The shape of the surrounding bone and the position of the molar roots were used as landmarks to obtain the same stages of development for different animals. The mineral density was quantified at two locations throughout the enamel thickness: at the

central and mesial/lateral side of the enamel. At each region three locations were selected: outer enamel (OE), mid-enamel (ME, half way between enamel surface and dentin-enamel junction DEJ), and inner enamel (IE, near DEJ) (Clementino- Luedemann & Kunzelmann, 2006) (Fig. 3m). For human teeth density measurements (expressed as mg hydroxyapatite/cm^3) were made at 540 micrometer intervals and plotted for each tooth individually (slice number). For mouse incisors beginning at the apical part and moving toward the tip, cross-sectioned images were collected at sequential intervals of 300 µm in maturation- stage and 60 µm in secretory-stage enamel. In wild-type mandibular incisors, enamel maturation begins approximately at the level where an imaginary line drawn between first and second molars intersects the incisor; in that area, the mineral density of secretory-stage enamel equals that of dentin (approximately 1,300 mg HA/cm^3), and the dentin layer is around 100 µm wide. All the teeth (mouse and human) were run by the same Micro-CT and operated and calculated by the same individuals.

Measurement of enamel thickness

The teeth were scanned with an EasyTom Micro-CT (RX Solutions, France) at the Centre de Microtomographie (IC2MP, iPHEP, University of Poitiers). During the scanning procedure beam intensity was set at 70KV and tube current at 230 µA. Each molar was acquired with 992 projections resulting in 1299 slices using cone-beam reconstruction algorithm. The isovoxel size was set to 0.015 mm. High-resolution micro-computed tomography (HR-µCT) images taken of the original molars were used to compute virtual 3D models of the enamel cap. The crown enamel volume data was converted into a polygonal surface, a 3D irregular array of contiguous triangles corresponding to a set of tridimensional points or nodes connected by edges (Guy, Gouvard, Boistel, Euriat, & Lazzari, 2013). This operation allowed the partition of the crown enamel into its inner (enamel-dentin-junction; EDJ) and outer (outer enamel surface; OES) components. For each molar, linear mesial, occlusal and lateral enamel thickness was measured following procedures developed by (Guy, Gouvard, Boistel, Euriat, & Lazzari, 2013). Mesio-distal and bucco-lingual dimensions of the teeth were measured according to the method described before (Moorrees, Thomsen, Jensen, & Yen, 1957). The thickness of the incisor enamel layer was measured as the shortest distance from the line perpendicular from dentin- enamel junction (DEJ) to the enamel surface.

Statistical analysis

All values are presented as means ± standard error of mean (SEM). Data were analyzed using an unpaired Student t test with $p<0.05$ was considered statistically significant.

RESULTS

Quantification of white spots on occlusal surface of human fluorotic molars by QLF

First, the enamel was examined for defects visually under white light using a stereo microscope (4-10x). In TF-I/II and control group no white spots were apparent when enamel was examined wet. After drying, chalky-white spots became visible on the teeth TIFI/II but not in the Amsterdam non-fluorotic control group. In TF-III/IV group the chalky-white areas were visible both wet and after drying (Fig. 1a, b). Also with 4-10x magnification we did not find any pits or irregularities in the enamel surface of either TF-I/II or TF-III/IV groups.

Subsequently, the occlusal surfaces of the molars were examined by QLF, a technique with which defects are seen as non-fluorescent (dark) areas (Fig. 1d). Using QLF, the TF-III/IV group contained a 4.5 fold higher score (45%±5% of the occlusal surface, n=4) as the TF-I/II group (10%±3%, n=4) (Fig. 1c-e). No non-fluorescent areas could be seen with QLF in the Amsterdam non-fluorotic control group (data not shown).

Hypomineralization in human fluorotic enamel measured by Micro-CT

Micro-CT was used to determine the effect of fluoride on enamel mineral content. It is a noninvasive method which allows virtual sectioning of the teeth. The 3D image analytical tools offer the opportunity to characterize the morphology and properties of dental tissue in a quantitative way.

Mineral density measurements in 3D-reconstructed molar models showed the highest density in the tip of the cusps of the control teeth (most calcified) and a decrease in cervical direction and toward fissure base. Although the fluorotic teeth followed the same pattern, the cusp tips were less mineralized. Moreover, the higher the TF index grade the more areas were found that halfway the cusp height were less mineral dense (both lingually and buccally; Fig.2b,c,d respectively). Weak hypermineralized lines were noticed in fluorotic teeth (black arrows in Fig 2 f,g,h)

In human TF-III/IV molars the enamel of the cervical region near Cement-Enamel Junction (CEJ) appeared to be the least mineralized (red arrows in Fig. 2h). Hypomineralized subsurface layers were detected in fluorotic enamel of TF-III/IV upper molars (Fig. 2d). In cross-sections through these areas, the subsurface defects seemed to be relatively superficial without extending deeper (Fig. 2h). In deeper layers multiple weak hypermineralized lines separated by hypomineralized areas ran parallel to the hypomineralized surface (Fig. 2h).

Fig. 2k shows the distribution of mineral density in human fluorotic enamel from the outer to the inner enamel layer in the control group (n=3), and the TIF-I/II (n=6) and TIF-III/IV (n=6) groups represented as 3D line plots. In both fluorotic and control groups, the lowest density was near DEJ (Dentin-Enamel-junction) but density increased from DEJ towards the

outer enamel surface (Fig. 2j). However, in human fluorotic enamel at different depths the mineral densities between the three groups (control and the two fluorotic groups) did not show statistical differences (Fig.2j).

Hypomineralization in mouse fluorotic enamel measured by Micro-CT

Virtual reconstruction of fluorotic enamel in the developing mouse incisor showed that the changes seen at the enamel surface were developmental-stage dependent; at late maturation fluorotic mouse enamel exhibited basically the same enamel defects as human TF-III enamel (a patchy distribution of hypomineralized subsurface; hypermineralized areas at various depths of the enamel layer and the enamel near the CEJ markedly less mineralized Fig. 3e-h; Fig. 2f). At early maturation mouse fluorotic enamel showed a surface that was hypermineralized with a hypomineralized subsurface and weak hypermineralized patchy areas (Fig. 3f).

In developing mouse incisors mineral density in control and fluorotic enamel increased in sigmoidal pattern from secretory to the late maturation (Fig. 3k). In fluorotic mice enamel the slope of the mineral increase became steeper at the onset of early maturation (Fig. 3k).

Quantification of the mineral density in mouse enamel showed that the distribution patterns of density differed between fluorotic and control groups including (Fig. 3j): (1) a 31% reduction ($p<0.0001$) in the total mineral density at the maturation stage in fluorotic mice. (2) A 9% ($p=0.004$) lower mineral density of maturation enamel mesially and laterally than centrally in fluorotic enamel but not in wild-type enamel. (3) Unlike to human, in mouse fluorotic enamel the proportion of changes in mineral density was the same in outer (OE), mid (ME) and inner (IE) enamel, all reduced by ~30% ($P= <0.0001$).

Enamel thickness and crown size in human fluorotic enamel measured by Micro-CT

To investigate the effect of fluoride on enamel thickness in fluorotic human teeth, we made virtual slices through the mesial cusps and measured linear thickness in three regions (cusp tip, maximum occlusal and maximum lateral thickness) (Fig. 4a-i). The first upper molar tooth was excluded for its crown shape was different from other teeth. The differences in enamel layer thickness between TF-I/II and TF-III/IV are summarized in box plots (Fig. 4e,f). In TF-III/IV teeth, the average occlusal enamel layer was approximately 10% thinner at the buccal side (Fig 4i) and 14% thinner at the lingual side (Fig 4h) in comparison to TF-I teeth but values were not statistically significant.

The crown size of the most fluorotic human molars differed from that of the least fluorotic molars measured occlusally as the mesio-distal (black arrow in Fig. 4g) and bucco-

lingual length (red arrow in Fig. 4g). The mesio-distal length of the TF-III/IV group was significantly smaller than those of TF-I/II group (18%; P=0.02; Fig4i); no differences were detected in the bucco-lingual size between the two groups (Fig. 4h). In fluorotic mice the enamel layer of the incisor was 7% thinner than in control mice but was not statically significant (p=0.5) (Fig. 4k, l)

DISCUSSION

Currently, in 40 countries fluoride is added to the drinking water as cariostatic agent. Where water fluoridation is not possible, salt fluoridation is used as a next-best option. Based on the study in major Colombian cities, the mean total daily fluoride intake (mg F/day), from salt (180- 220 mg F/ kg), water (0.08 ppm) and toothpaste, was the highest in children in Medellina and Bogota (1.73 and 1.43 respectively) (100). In the Netherlands since 1976 no fluoride is added to the drinking water. Therefore, teeth from Amsterdam subjects were used as non-fluorotic controls group to compare the mineral distribution with that in the fluorotic group from Bogota.

To the best of our knowledge no quantified Micro-CT data have been published to examine mineralization defects in human fluorotic enamel. Micro-CT analysis of non-fluorotic human molars showed that mineral-density in the cusp tips was higher than enamel in the other parts. In human fluorotic enamel we found hypermineralized patches and weak lines. We cannot exclude the possibility that some lines (e.g. with orientation different from the usual growth lines) are artefacts. Many lines in human fluorotic enamel resembled the lines seen in fluorotic enamel of rodents chronically exposed to low doses of fluoride or injected with a high dose of fluoride and examined by different techniques (Transmission Electron Microscopy, microradiography and backscatter scanning electromicroscopy; (31, 86, 93, 101). The data suggest that enamel mineral defects in human fluorotic enamel are similar to those in fluorotic mouse enamel.

In mature (impacted) human fluorotic enamel we found that the surface enamel was not hypermineralized. In fluorotic mouse enamel using backscatter scanning electron microscopy the enamel surface appeared hypermineralized only at early maturation after which these lines became obscured by ongoing mineral deposition (89). The difference in surface hypermineralization between human and mouse fluorotic enamel could be due to (1) differences in resolution of the technique used (SEM, Micro-CT) ;(2) changes in the rate of enamel development that is higher in rodent incisors than in human teeth; (3) differences in developmental stages, exposure time and in F dose.

Enhanced hypermineralization of surface enamel and more pronounced hypermineralization lines in mouse incisors were found when secretion of bicarbonates by ameloblasts was disrupted (i.e. in *Ae2*$^{-/-}$ mice) suggesting that effective buffering reduces

fluorotic changes(89). The present observation that also human fluorotic TF-IV enamel was diffusely hypomineralized but contained weak hypermineralized lines or small areas that were hypermineralized suggests that - similar to rodents - also in developing human fluorotic enamel fluoride transiently accelerates mineral formation, causing a local acidification of enamel. Further evidence that hypermineralization could take place in developing fluorotic human enamel is suggested by slightly elevated (not statistically significant) levels of phosphorus detected by micro-Raman spectrophotometry.

We did not measure in human teeth the occurrence of areas with different pH or changes in size of these areas in fluorotic enamel which requires a different approach. In fluorotic rats and mice modulation bands are wider after staining with pH dye solutions suggesting fluorotic enamel is more acidic (51) possibly due to stimulation of hypermineralization by fluoride(102). In secretory stage enamel, this acidification may be buffered by binding to amelogenins present in excess but at maturation stage by secretion of bicarbonates by ameloblasts in exchange for Cl^- (53, 74). During long term exposure to fluoride the ongoing demand to secrete more buffer likely depletes Cl^- levels in enamel, reduces the capacity of ameloblasts to secrete bicarbonates, delays ameloblast modulation and eventually results in an overall hypomineralization (97). Interestingly analysis of human fluorotic teeth by secondary ion mass spectrometry and X-ray microanalysis showed the same compositional changes in the superficial layers as reported in fluorotic mouse enamel: reduction in Cl^- level, along with a slight increase in K^+ and F^- (103). These similarities suggest the same mechanisms leading to fluorotic enamel are operating in humans and in rodents.

Our results furthermore showed that a moderate daily dose of fluoride to children with developing enamel slightly (but not significantly) reduced the thickness of enamel in mesial cusps along with a (statistically significant) decrease of mesio-distal length of the tooth also reported by others (95, 104). Reduction of the thickness of enamel in rodents was correlated by fluoride-induced accumulation of matrix and its intracellular degradation(105). The results of the current study can be interpreted as indirect evidence that the primary effect of fluoride on enamel formation is stimulation of mineral formation which releases excess of protons to which ameloblasts immediately respond.

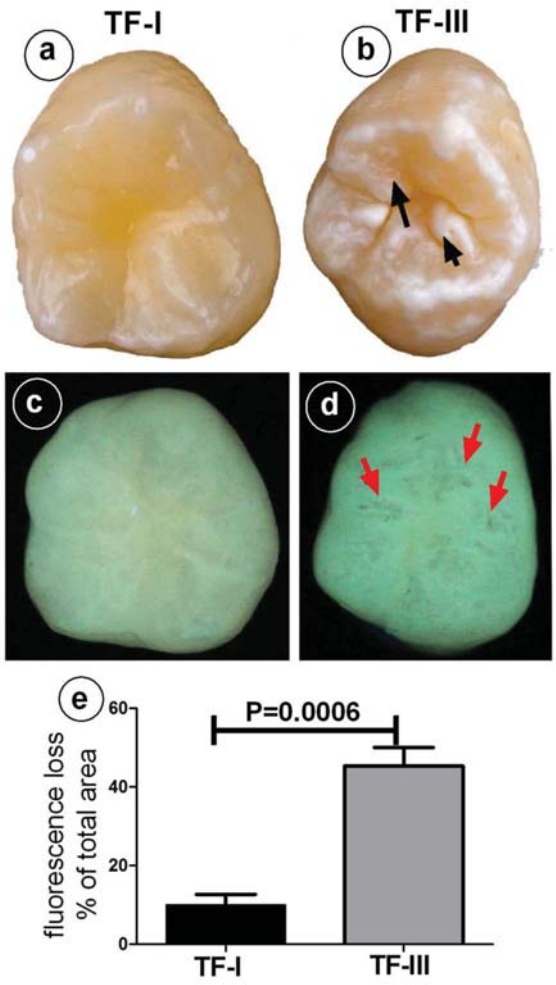

Fig 1. Enamel surface defects in response to fluoride measured by QLF. (a,b) occlusal view of bright light image of molars with white spots in non-plaque retention areas (black arrows in (b)). (c,d) QLF image showing less mineralized areas (red arrows in (d)). (e) shows the summary of QLF measurements (n=6 for each group)

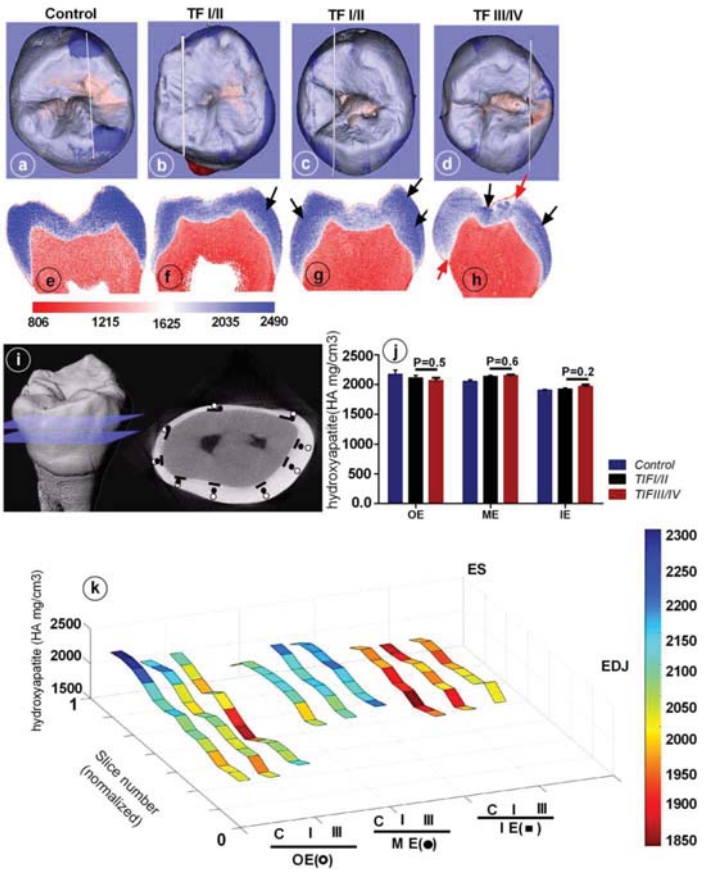

Fig 2. Enamel mineral density in human fluorotic enamel determined by Micro-CT Fig. (a-d) occlusal view of 3-D reconstruction model for control (a), TF-I/II (b,c) and TF-III/IV (d) scored teeth. (e-h) micro-CT images from a longitudinal section through selected areas (showed by white lines in 3-D reconstructed images (a-d)). Black arrows indicate hypermineralized and red arrows indicate less mineralized areas. The color bar represents the relative mineral values of the Micro-CT images (~800-2500 mg HA/cm^3). (i) is a schematic 3D Micro-CT reconstruction image of selected regions in enamel. Open circles, closed circles and lines represent the areas of measurement in outer enamel (OE), mid enamel (ME) and inner enamel (IE), respectively. (j) Bar diagrams showing mean value of enamel mineral density in control (n=3), TF-I/II (n=6) and TF-III/IV (n=6) teeth. (k) is a 3-D ribbon plot of changes in mineral density from enamel surface (ES) to dentin enamel junction (DEJ) in control (n=3), TF- I/II (n=6); and TF-III/IV enamel (n=6); distance between slices (0.5 mm). E, enamel; D, dentin. Note: red contour lines near the enamel surface (see (e-h)) have been excluded for all the measurements

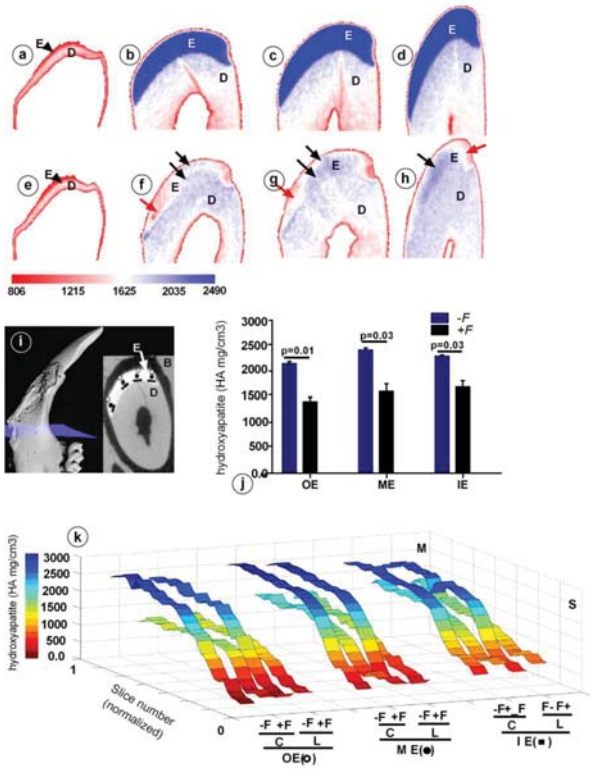

Fig 3. Mineral density in fluorotic mouse enamel from secretory stage (S, right, red) to fully mature (M) enamel (blue). (a-d) developmental changes in mineral density in sections through sound enamel of a mandibular incisor of a non-fluorotic control mouse (increase of development from left to right). (e-h) show the density in enamel in sections of a fluorotic incisor. Black arrows indicate hypermineralized and red arrows indicate less mineralized areas. The color bar represents the relative mineral values of the Micro-CT images (~800-2500 mg HA/cm^3). (i) schematic 3D Micro-CT reconstruction image and selected regions in enamel. The light purple sheet represents plane of sectioning. Open circles, closed circles and lines represent the areas of measurement in outer enamel (OE), mid enamel (ME) and inner enamel (IE), respectively. (j) bar diagrams showing the changes in *mean value* of enamel mineral density at *late maturation* (just prior to eruption) in central (C) and the lateral sides (L) between control non-fluorotic (-F) and fluorotic (+F) teeth. (o) are a 3-D ribbon plots illustrating the changes in mineral density from early secretory to late maturation stage measured at the enamel surface (OE), near the dentin enamel junction (IE) and half way in between (ME). Different densities have been shown by different colors (reference bar; -F: non-fluorotic; +F: fluorotic; distance between slices (0.5 mm). E, enamel; D, dentin. Note: red contour lines in (a-d; e-h) are artificial lines and (as for Fig 2d-f) have been excluded from the measurements.

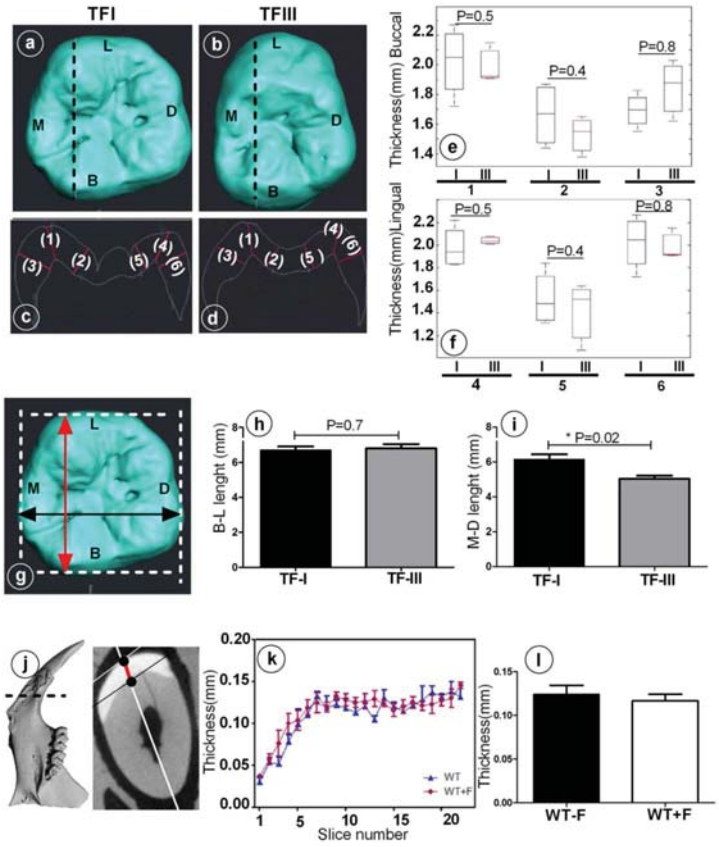

Fig 4. Enamel thickness (a-f) and crown size (g-i) of fluorotic human molars (TF-I and TF-III) and enamel thickness in fluorotic and nonfluorotic controls mouse incisor. (j-l) human enamel thickness at the cusp tip taken from the EDJ to the most superior tip on the OES cusp contour in *buccal* (B) side (Fig c [1], Fig 4d [1] and *lingual* (L) side (Fig 4c [4], Fig 4d [4]). The maximal occlusal thickness taken perpendicular to a line drawn from the EDJ cusp tip to the longitudinal groove of the EDJ occlusal base from buccal (Fig 4c [2], Fig 4d [2] and lingual (Fig 4c [5], Fig 4d [5]) sides. Maximum lateral thickness, taken as the maximum 'radial' thickness measured from any point of the EDJ lateral crown face in buccal side (Fig 4c [3]; Fig 4d [3]) and lingual side (Fig 4c [6], Fig 4d [6]. Box plots represent enamel thickness in mm (TF- I and TF-III) of the mesial cusp section (e,f). Extension of bucco-lingual distance is indicated by double pointed red arrow (g) and the mesio (M)-distal (D) distance by double pointed black arrow (g) for TF-I and TF-III molars (g). Enamel thickness in mouse mandibular incisors was measured from the early secretory stage toward end of maturation stage (j). The figure (k) and bar diagram (l) represents the thickness differences between non-fluorotic wild-type (WT-F) and fluorotic wild-type (WT+F) teeth at progressive stages of enamel development and mature (k).

Chapter 6

General discussion

Dental enamel is mineralized by deposition of massive amounts of hydroxyapatite crystals formed from calcium and phosphate ions during enamel formation. At early secretory stage these crystals are initiated in a protein-rich matrix, and grow in length till late secretory stage when the enamel layer reaches its full thickness. During maturation stage the enamel matrix is degraded, the peptide fragments removed and the matrix replaced by minerals until mineralization is completed (2). Each unit of hydroxyapatite crystal [$Ca_{10}(PO4)_6.2OH$] formed during this process releases ~8 H^+ protons ions into the enamel matrix space. In theory, this process results into a decrease in pH in the enamel matrix space, an effect that will peak in maturation stage when crystal formation enhances sharply. In order to deal with the drop in pH, the enamel ameloblasts have been proposed to buffer acid using bicarbonate (18, 25, 33, 51, 55). Ameloblasts are apically tightly bound to each other by (tight) junctional complexes. These complexes are assumed to prevent or restrict paracellular entry to the enamel space (106). To transport bicarbonate and other ions across the ameloblast layer into forming enamel requires the activity of exchanger(s) and/or transporter(s) located in apical, basal or basolateral plasma membranes.

At the start of the studies described in this thesis published data suggested that maturation ameloblast regulate pH by secretion of $HCO3^-$ mediated by $Cl^-/HCO3^-$ exchangers of the family located in the apical plasma membrane. The bicarbonate was thought to be either generated by cytosolic carbonic anhydrase and/or imported by Na^+-bicarbonate cotransporters in the basolateral membranes (Fig.1) (33, 55, 107). To operate apical $Cl^-/HCO3^-$ exchangers in ameloblasts the enamel should contain sufficient amounts of chloride which is provided by maturation ameloblasts by passing large amounts of chloride into the enamel by apical CFTR. In turn ameloblasts can import chloride by basolateral AE2 in exchange of bicarbonate. NHE1 at the basolateral membranes extrude H^+ in exchange for sodium (Fig 1) (14, 107).

The subject of this thesis was to address the expression profiles of various pH regulatory transporters in ameloblasts and the role played by these pH regulatory transporters, focusing on members of three transporter families, i.e. SLC4A4, SLC26A and NKCC1, in the events leading to enamel formation.

Previous studies by others had shown that patients with SLC4A4 mutations have enamel abnormalities seen as white-chalk-like spots (108). The NBCe1 mutations in these patients involved all three NBCe1 variants (*NBCe1*A-C). In vitro studies using the LS8 immortalized mouse ameloblast cell model had revealed that the *NBCe1-B* variant is expressed in the basolateral membranes. Moreover, the level of *NBCe1-B* mRNA is regulated by pH, with the highest level of mRNA expression at acid pH (40).

In **Chapter 2**, we examined the expression of Na-Bicarbonate exchanger 1 (Nbce1) using antibodies that distinguish the two different NBCe1 (SLC4A4) splice variants to

analyze their localization in ameloblasts both at the mRNA and the protein level. Nbce1 protein expression depended on developmental stage: low expression in secretory stage, no expression in early maturation ameloblasts and re-expression by advanced maturation ameloblasts. The expression in ameloblasts alternated with that in the papillary layer. Without functional NBCe1 (in *Nbce1*$^{-/-}$ mice) the mineral density of enamel was strongly reduced. We found that mineral density of enamel in *Nbce1*$^{-/-}$ teeth was lower. In *CFTR*$^{-/-}$ and *Ae2*$^{-/-}$ mice the expression of Nbce1 protein in enamel organs was strongly elevated. The data favored a role of Nbce1 in pH regulation by responding to acids (55).

Strong apical immunostaining of maturation ameloblasts for SLC26A4 (pendrin) had suggested in an earlier study the possible role of this exchanger in transporting intracellular bicarbonate into enamel. However, in *pendrin*$^{-/-}$ mice enamel formation was normal. We hypothesized that in *pendrin*$^{-/-}$ mice bicarbonate generated by carbonic anhydrase activity or transported by NBCe1 likely can be exchanged for Cl^- by other family members of pendrin, SLC26A3/ Dra SLC26A6/PAT1 operating in ameloblasts. In **Chapter 3** we showed that SLC26A3/Dra and SCL26A6 are indeed expressed and are localized in the apical membranes of the ameloblasts. However, both *Dra*$^{-/-}$ or *Slc26a6*$^{-/-}$ mice had a normal dental or skeletal phenotype and showed no changes in mineral density, as measured by micro-computed tomography. Western blot analysis indicated that enamel organ of *Slc26a6*$^{-/-}$ mice contained elevated levels of Dra and pendrin protein. Similar results were obtained for SLC26a1 by Yin et al: apical expression was seen in maturation ameloblast, enamel formation was not changed in *SLc26a1*$^{-/-}$ mice but the number of transcripts for Slc26a6 and Slc26a2, Nbce1 and CFTR in the *Slc26a1*$^{-/-}$ enamel were elevated (75). Therefore, it is reasonable to conclude that there are strong compensatory reactions in response to the deletion of one of the members SLC26A family (i.e. SLC26A1, SLC26A3, SlC26A4, SLC26A6). A possible strategy to test for the function of Slc26A family is by deleting several members to reduce compensation. However, mouse embryos with double knockout for Dra and Slc26a6 are not viable and die intrauterine. An alternate approach would be to inhibit expression of two or more transporters at the transcriptional level and measure pH in cultured ameloblasts to disclose their function in ameloblasts.

The relevance of Cl^- in forming enamel was clear by microprobe X-ray analysis indicating accumulation of Na^+ and K^+ and reduction of Cl^- in hypomineralizing maturation stage enamel in *CFTR*$^{-/-}$ and *Ae2*$^{-/-}$ mice (18). In **Chapter 4** we tested the hypothesis that Na^+:K^+:2Cl^- (NKCC1) cotransporter family is responsible for Na^+ and K^+ removal from the enamel space. Our results showed that in mice Nkcc1 is expressed in the papillary layer but not in the ameloblast layer.

The height of dental epithelium in upper incisors of Nkcc1$^{-/-}$ mice at advanced maturation was shorter and enamel mineral density was slightly lower than in wild-type

controls. The enamel organ of Nkcc1$^{-/-}$ mice contained more pendrin, Slc26a6 and Nbce1 protein suggesting compensation of Nkcc1 mutation. To study whether the Nkcc1 is functional in ameloblasts, we examined effects of bumetanide (an inhibitor of NKCCs) on cell volume in ameloblast-like HAT-7 cell cultures. The regulation of cell volume was impaired by bumetanide, indicating that NKCC1 is capable of significantly contributing to cell volume regulation of the enamel organ and papillary layer.

Based on the studies discussed in this thesis a more complete model for ion and bicarbonate transport into/out of the enamel space has been proposed (Fig.1) which takes us a step closer toward understanding the mechanism underling enamel hypomineralization. Most of these studies are descriptive and give no functional proof. To present functional evidence requires electrophysiological studies either in whole-cell or in perforated patch-clamp using an N- cyanosulphonamide compound S0859 or DIDS, (a selective and a potent inhibitor of NBCs) or pharmacological inhibition of the transporter at the transcriptional level. The later approach would involve delivery of NBCe1 siRNA in ameloblasts to knockdown of the NBCe1 in the ameloblasts. In addition, pH measurements in cultured ameloblasts using pH-sensitive dyes will help assess how this transporter contributes to extra- and intracellular pH changes. Our group recently started to perform functional studies testing if functional NBCe1 in ameloblast is involved by loading cells either with acid (to examine whether the NBCe1 is an acid extruder) or with alkali (to examine whether the NBCe1 is an acid loader) and whether the recovery from an acid/alkali load is blocked by DIDS (74). The results indicate that when DIDS was added, the degree of alkalinization was reduced and occurred slower than in controls indicating that a basolateral $HCO3^-$ transporter, most probably NBCe1/SLC4A4, has an important role in $HCO3^-$ uptake (74). A more challenging approach to these studies is to subject ameloblasts isolated from the *Nbce1*$^{-/-}$ mice to an acid/alkali load in order to examine whether the recovery from acid/alkali loads is decreased in the knockout compared to the wild-type.

Finally, we examined whether enamel fluorosis is the result of transient disruption of pH regulation. Fluoride accelerates hydroxyapatite formation which enhances release of protons. In developing enamel proton production could exceed the buffering capacity of ameloblasts which results in local acidification (89). In **Chapter 5** we examined human fluorotic molars for presence of hypermineralized lines to test the possibility that during exposure to fluoride increased proton release in forming enamel also happens in humans. Our micro-CT study shows that exposure of mice and humans to fluoride basically gives the same effect in developing enamel: formation of hypomineralized enamel with presence of hypermineralized lines. The development of these defects may be explained by selective dissolution of crystallites at the maturation stage by protons released during hypermineralization at the surface. These protons could dissolve immature crystals in the

subsurface, particularly in the maturation stage when the ruffle-ended bands are acidic and the mineralization front is stationary, exposing the same surface area repeatedly to fluoride insults.

Taken together, the comprehensive studies and analyses that were done and presented in my PhD thesis helps to better understand the unique interactions between the mineralizing enamel extracellular matrix and the ameloblasts that direct these processes. With these studies, the paradigm for understanding of the interactions between ameloblast function and matrix biology can be advanced.

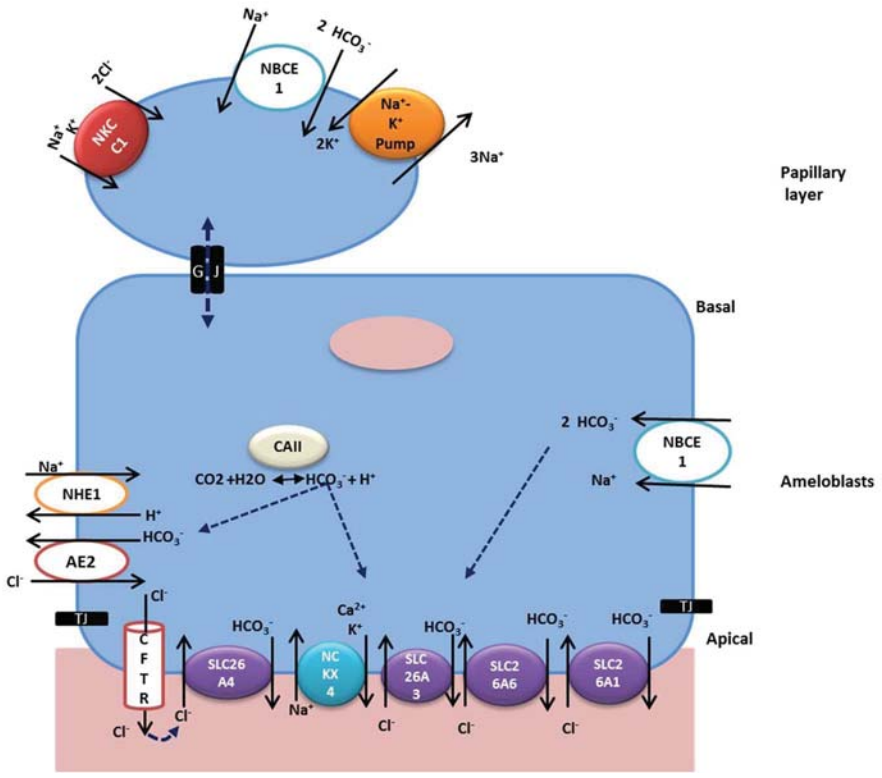

Fig 1. Model for transepithelial ion transport by maturation ameloblasts. $HCO3^{-}$ mediated by Car2 (109) may extrude via pendrin, Dra(SLC26A3), SLC26A6 (Pat1), SLC26A1 (33, 75, 110) or yet an unknown transporter to the enamel space. In ameloblast Cl^{-} is extruded by CFTR (53) and exchange by SLC26A6 for $HCO3^{-}$ needed for hydroxyapatite formation. Calcium needed for hydroxyapatite formation, maybe transported out of the cells at the apical pole by at least one of the NCKX members of sodium-calcium-potassium exchangers (NCKX4) (37). GJ, gap junction; TJ, tight junction.

References

1. Smith CE, Nanci A. Protein dynamics of amelogenesis. The Anatomical Record. 1996;245(2):186-207.
2. Smith C. Cellular and chemical events during enamel maturation. Critical Reviews in Oral Biology & Medicine. 1998;9(2):128-61.
3. Nanci A. Ten Cate's Oral Histology Development, Structure, and Function, 8/e: Elsevier India; 2012.
4. Fincham A, Moradian-Oldak J, Simmer J. The structural biology of the developing dental enamel matrix. Journal of Structural Biology. 1999;126(3):270-99.
5. Robinson C, Kirkham J, Briggs H, Atkinson P. Enamel proteins: from secretion to maturation. Journal of Dental Research. 1982:1490-5.
6. Gibson CW, Yuan Z-A, Hall B, Longenecker G, Chen E, Thyagarajan T, et al. Amelogenin-deficient mice display an amelogenesis imperfecta phenotype. Journal of Biological Chemistry. 2001;276(34):31871-5.
7. Moradian-Oldak J, Paine M, Lei Y, Fincham A, Snead M. Self-assembly properties of recombinant engineered amelogenin proteins analyzed by dynamic light scattering and atomic force microscopy. Journal of Structural Biology. 2000;131(1):27-37.
8. Rauth RJ, Potter KS, Ngan AY-W, Saad DM, Mehr R, Luong VQ, et al. Dental enamel: genes define biomechanics. Journal of the California Dental Association. 2009;37(12):863.
9. Smith CE, Chong DL, Bartlett JD, Margolis HC. Mineral acquisition rates in developing enamel on maxillary and mandibular incisors of rats and mice: implications to extracellular acid loading as apatite crystals mature. Journal of Bone and Mineral Research. 2005;20(2):240-9.
10. Inage T, Shimokawa H, Teranishi Y, Iwase T, Toda Y, Moro I. Immunocytochemical demonstration of amelogenins and enamelins secreted by ameloblasts during the secretory and maturation stages. Archives of Histology and Cytology. 1989;52(3):213-29.
11. Josephsen K, Fejerskov O. Ameloblast modulation in the maturation zone of the rat incisor enamel organ. A light and electron microscopic study. Journal of Anatomy. 1977;124(Pt 1):45.
12. Bonar LC, Shimizu M, Roberts JE, Griffin RG, Glimcher MJ. Structural and composition studies on the mineral of newly formed dental enamel: A chemical, X-ray diffraction, and 31p and proton nuclear magnetic resonance study. Journal of Bone and Mineral Research. 1991;6(11):1167-76.
13. Reith EJ, Boyde A. The arrangement of ameloblasts on the surface of maturing enamel of the rat incisor tooth. Journal of Anatomy. 1981;133(Pt 3):381.

14. Josephsen K, Takano Y, Frische S, Praetorius J, Nielsen S, Aoba T, et al. Ion transporters in secretory and cyclically modulating ameloblasts: a new hypothesis for cellular control of preeruptive enamel maturation. American Journal of Physiology-Cell Physiology. 2010;299(6):C1299-C307.
15. Lacruz R, Smith C, Kurtz I, Hubbard M, Paine M. New paradigms on the transport functions of maturation-stage ameloblasts. Journal of Dental Research. 2013;92(2):122-9.
16. Hubbard MJ. Calcium transport across the dental enamel epithelium. Critical Reviews in Oral Biology & Medicine. 2000;11(4):437-66.
17. Toth K, Shao Q, Lorentz R, Laird D. Decreased levels of Cx43 gap junctions result in ameloblast dysregulation and enamel hypoplasia in Gja1Jrt/+ mice. Journal of Cellular Physiology. 2010;223(3):601-9.
18. Bronckers A, Lyaruu D, Jalali R, Medina J, Zandieh-Doulabi B, DenBesten P. Ameloblast modulation and transport of Cl−, Na+, and K+ during amelogenesis. Journal of Dental Research. 2015;94(12):1740-7.
19. Wen X, Lacruz RS, Smith CE, Paine ML. Gene-expression profile and localization of Na+/K+-ATPase in rat enamel organ cells. European Journal of Oral Sciences. 2014;122(1):21-6.
20. Nurbaeva MK, Eckstein M, Concepcion AR, Smith CE, Srikanth S, Paine ML, et al. Dental enamel cells express functional SOCE channels. Scientific Reports. 2015;5.
21. Hu P, Lacruz RS, Smith CE, Smith SM, Kurtz I, Paine ML. Expression of the sodium/calcium/potassium exchanger, NCKX4, in ameloblasts. Cells Tissues Organs. 2012;196(6):501-9.
22. Duan X. Ion channels, channelopathies, and tooth formation. Journal of Dental Research. 2014;93(2):117-25.
23. Kurisu K, Tabata M. Human genes for dental anomalies. Oral Diseases. 1997;3(4):223-8.
24. Wright JT, Hart TC, Hart PS, Simmons D, Suggs C, Daley B, et al. Human and mouse enamel phenotypes resulting from mutation or altered expression of AMEL, ENAM, MMP20 and KLK4. Cells Tissues Organs. 2009;189(1-4):224-9.
25. Lyaruu D, Bronckers A, Mulder L, Mardones P, Medina J, Kellokumpu S, et al. The anion exchanger Ae2 is required for enamel maturation in mouse teeth. Matrix Biology. 2008;27(2):119-27.
26. Bronckers A, Kalogeraki L, Jorna HJ, Wilke M, Bervoets TJ, Lyaruu DM, et al. The cystic fibrosis transmembrane conductance regulator (CFTR) is expressed in maturation stage ameloblasts, odontoblasts and bone cells. Bone. 2010;46(4):1188-96.

27. DenBesten P, Thariani H. Biological mechanisms of fluorosis and level and timing of systemic exposure to fluoride with respect to fluorosis. Journal of Dental Research. 1992;71(5):1238-43.
28. Alaluusua S. Aetiology of molar-incisor hypomineralisation: a systematic review. European Archives of Paediatric Dentistry. 2010;11(2):53-8.
29. Pindborg JJ. Aetiology of developmental enamel defects not related to fluorosis. International Dental Journal. 1982;32(2):123-34.
30. Atar M, Körperich EJ. Systemic disorders and their influence on the development of dental hard tissues: a literature review. Journal of Dentistry. 2010;38(4):296-306.
31. Angmar-Månsson B, Ericsson Y, Ekberg O. Plasma fluoride and enamel fluorosis. Calcified Tissue Research. 1977;22(1):77-84.
32. Parry DA, Poulter JA, Logan CV, Brookes SJ, Jafri H, Ferguson CH, et al. Identification of mutations in SLC24A4, encoding a potassium-dependent sodium/calcium exchanger, as a cause of amelogenesis imperfecta. The American Journal of Human Genetics. 2013;92(2):307-12.
33. Bronckers AL, Guo J, Zandieh-Doulabi B, Bervoets TJ, Lyaruu DM, Li X, et al. Developmental expression of solute carrier family 26A member 4 (SLC26A4/pendrin) during amelogenesis in developing rodent teeth. European Journal of Oral Sciences. 2011;119(s1):185-92.
34. Toyosawa S, Ogawa Y, Inagaki T, Ijuhin N. Immunohistochemical localization of carbonic anhydrase isozyme II in rat incisor epithelial cells at various stages of amelogenesis. Cell and Tissue Research. 1996;285(2):217-25.
35. Lyaruu D, Bervoets T, Bronckers A. Short exposure to high levels of fluoride induces stage-dependent structural changes in ameloblasts and enamel mineralization. European Journal of Oral Sciences. 2006;114(s1):111-5.
36. Parker MD, Boron WF. The divergence, actions, roles, and relatives of sodium-coupled bicarbonate transporters. Physiological Reviews. 2013;93(2):803-959.
37. Lacruz RS, Nanci A, Kurtz I, Wright JT, Paine ML. Regulation of pH during amelogenesis. Calcified Tissue International. 2010;86(2):91-103.
38. Lee S-K, Boron WF, Parker MD. Substrate specificity of the electrogenic sodium/bicarbonate cotransporter NBCe1-A (SLC4A4, variant A) from humans and rabbits. American Journal of Physiology-Renal Physiology. 2013;304(7):F883-F99.
39. Simmer J, Fincham A. Molecular mechanisms of dental enamel formation. Critical Reviews in Oral Biology & Medicine. 1995;6(2):84-108.
40. Paine ML, Snead ML, Wang H, Abuladze N, Pushkin A, Liu W, et al. Role of NBCe1 and AE2 in secretory ameloblasts. Journal of Dental Research. 2008;87(4):391-5.

41. Lyman GE, Waddell WJ. pH gradients in the developing teeth of young mice from autoradiography of [14C] DMO. American Journal of Physiology-Renal Physiology. 1977;232(4):F364-F7.
42. Bernardo AA, Bernardo CM, Espiritu DJ, Arruda JA, editors. The sodium bicarbonate cotransporter: structure, function, and regulation. Seminars in nephrology; 2006: Elsevier.
43. Romero MF, Chen A-P, Parker MD, Boron WF. The SLC4 family of bicarbonate transporters. Molecular Aspects of Medicine. 2013;34(2):159-82.
44. Gawenis LR, Bradford EM, Prasad V, Lorenz JN, Simpson JE, Clarke LL, et al. Colonic anion secretory defects and metabolic acidosis in mice lacking the NBC1 cotransporter. Journal of Biological Chemistry. 2007;282(12):9042-52.
45. Wright J, Hall K, Grubb B. Enamel mineral composition of normal and cystic fibrosis transgenic mice. Advances in Dental Research. 1996;10(2):270-5.
46. Zheng L, Zhang Y, He P, Kim J, Schneider R, Bronckers A, et al. NBCe1 in mouse and human ameloblasts may be indirectly regulated by fluoride. Journal of Dental Research. 2011;90(6):782-7.
47. Snead CM, Smith SM, Sadeghein N, Lacruz RS, Hu P, Kurtz I, et al. Identification of a pH-responsive DNA region upstream of the transcription start site of human NBCe1-B. European Journal of Oral Sciences. 2011;119(s1):136-41.
48. Sasaki S, Takagi T, Suzuki M. Cyclical changes in pH in bovine developing enamel as sequential bands. Archives of Oral Biology. 1991;36(3):227-31.
49. Bevensee MO, Schmitt BM, Choi I, Romero MF, Boron WF. An electrogenic Na+-HCO 3− cotransporter (NBC) with a novel COOH-terminus, cloned from rat brain. American Journal of Physiology-Cell Physiology. 2000;278(6):C1200-C11.
50. Uriarte I, Banales JM, Sáez E, Arenas F, Oude Elferink RP, Prieto J, et al. Bicarbonate secretion of mouse cholangiocytes involves Na+-HCO 3− cotransport in addition to Na+-independent Cl−/HCO3− exchange. Hepatology. 2010;51(3):891-902.
51. Bronckers A, Lyaruu D, DenBesten P. The impact of fluoride on ameloblasts and the mechanisms of enamel fluorosis. Journal of Dental Research. 2009;88(10):877-93.
52. Garant PR, Sasaki T. Ultracytochemistry of ouabain-sensitive K+-dependent p-nitrophenyl phosphatase in rat incisor enamel organ. The Anatomical Record. 1986;216(1):1-9.
53. Bronckers AL, Lyaruu DM, Guo J, Bijvelds MJ, Bervoets TJ, Zandieh-Doulabi B, et al. Composition of mineralizing incisor enamel in cystic fibrosis transmembrane conductance regulator-deficient mice. European Journal of Oral Sciences. 2015;123(1):9-16.

54. Gawenis LR, Greeb JM, Prasad V, Grisham C, Sanford LP, Doetschman T, et al. Impaired gastric acid secretion in mice with a targeted disruption of the NHE4 Na+/H+ exchanger. Journal of Biological Chemistry. 2005;280(13):12781-9.
55. Jalali R, Guo J, Zandieh-Doulabi B, Bervoets T, Paine M, Boron W, et al. NBCe1 (SLC4A4) a potential pH regulator in enamel organ cells during enamel development in the mouse. Cell and Tissue Research. 2014;358(2):433-42.
56. Alper SL, Sharma AK. The SLC26 gene family of anion transporters and channels. Molecular Aspects of Medicine. 2013;34(2):494-515.
57. Trezise AE, Buchwald M. In vivo cell-specific expression of the cystic fibrosis transmembrane conductance regulator. Nature. 1991;353(6343):434.
58. Tizzano EF, Chitayat D, Buchwald M. Cell-specific localization of CFTR mRNA shows developmentally regulated expression in human fetal tissues. Human Molecular Genetics. 1993;2(3):219-24.
59. Zeng W, Lee MG, Yan M, Diaz J, Benjamin I, Marino CR, et al. Immuno and functional characterization of CFTR in submandibular and pancreatic acinar and duct cells. American Journal of Physiology-Cell Physiology. 1997;273(2):C442-C55.
60. Claass A, Sommer M, de Jonge H, Kälin N, Tümmler B. Applicability of different antibodies for immunohistochemical localization of CFTR in sweat glands from healthy controls and from patients with cystic fibrosis. Journal of Histochemistry & Cytochemistry. 2000;48(6):831-7.
61. Kawano S, Morotomi T, Toyono T, Nakamura N, Uchida T, Ohishi M, et al. Establishment of dental epithelial cell line (HAT-7) and the cell differentiation dependent on Notch signaling pathway. Connective Tissue Research. 2002;43(2-3):409-12.
62. Steward MC, Ishiguro H. Molecular and cellular regulation of pancreatic duct cell function. Current Opinion in Gastroenterology. 2009;25(5):447-53.
63. Soleimani M, Xu J, editors. SLC26 chloride/base exchangers in the kidney in health and disease. Seminars in nephrology; 2006: Elsevier.
64. Wall SM, Hassell KA, Royaux IE, Green ED, Chang JY, Shipley GL, et al. Localization of pendrin in mouse kidney. American Journal of Physiology-Renal Physiology. 2003;284(1):F229-F41.
65. Lohi H, Kujala M, Kerkelä E, Saarialho-Kere U, Kestilä M, Kere J. Mapping of five new putative anion transporter genes in human and characterization of SLC26A6, a candidate gene for pancreatic anion exchanger. Genomics. 2000;70(1):102-12.
66. Sindic A, Chang M-H, Mount DB, Romero MF. Renal physiology of SLC26 anion exchangers. Current Opinion in Nephrology and Hypertension. 2007;16(5):484-90.

67. Lamprecht G, Gaco V, Turner JR, Natour D, Gregor M. Regulation of the intestinal anion exchanger DRA (downregulated in adenoma). Annals of the New York Academy of Sciences. 2009;1165(1):261-6.
68. Höglund P, Haila S, Socha J, Tomaszewski L, Saarialho-Kere U, Karjalainen-Lindsberg M-L, et al. Mutations of the Down–regulated in adenoma (DRA) gene cause congenital chloride diarrhoea. Nature Genetics. 1996;14(3):316-9.
69. Jiang Z, Asplin JR, Evan AP, Rajendran VM, Velazquez H, Nottoli TP, et al. Calcium oxalate urolithiasis in mice lacking anion transporter Slc26a6. Nature Genetics. 2006;38(4):474.
70. Xia W, Yu Q, Riederer B, Singh AK, Engelhardt R, Yeruva S, et al. The distinct roles of anion transporters Slc26a3 (DRA) and Slc26a6 (PAT-1) in fluid and electrolyte absorption in the murine small intestine. Pflügers Archiv-European Journal of Physiology. 2014;466(8):1541-56.
71. Bronckers A, Guo J, Lyaruu D, Denbesten P, Zandieh-Doulabi B. Immunolocalization and western blotting of the anion exchanger pendrin in ameloblasts. European Journal of Oral Sciences. 2012;120(4):369-72.
72. Song Y, Yamamoto A, Steward MC, Ko SB, Stewart AK, Soleimani M, et al. Deletion of Slc26a6 alters the stoichiometry of apical Cl−/HCO 3− exchange in mouse pancreatic duct. American Journal of Physiology-Cell Physiology. 2012;303(8):C815-C24.
73. Ryu O, Hu C-C, Simmer J. Biochemical characterization of recombinant mouse amelogenins: protein quantitation, proton absorption, and relative affinity for enamel crystals. Connective Tissue Research. 1998;38(1-4):207-14.
74. Bori E, Guo J, Rácz R, Burghardt B, Földes A, Kerémi B, et al. Evidence for bicarbonate secretion by ameloblasts in a novel cellular model. Journal of Dental Research. 2016;95(5):588-96.
75. Yin K, Lei Y, Wen X, Lacruz RS, Soleimani M, Kurtz I, et al. SLC26A gene family participate in pH regulation during enamel maturation. PloS One. 2015;10(12):e0144703.
76. Glynn IM. A Hundred Years of Sodium Pumping. Annual Review of Physiology. 2002;64(1):1-18.
77. Gagnon F, Orlov SN, Tremblay J, Hamet P. Complete inhibition of Na+, K+, Cl− cotransport in Madin-Darby canine kidney cells by PMA-sensitive protein kinase. Biochimica et Biophysica Acta (BBA)-Biomembranes. 1998;1369(2):233-9.
78. Haas M. The Na-K-Cl cotransporters. American Journal of Physiology-Cell Physiology. 1994;267(4):C869-C85.
79. Evans RL, Park K, Turner RJ, Watson GE, Nguyen H-V, Dennett MR, et al. Severe impairment of salivation in Na+/K+/2Cl− cotransporter (NKCC1)-deficient mice. Journal of Biological Chemistry. 2000;275(35):26720-6.

80. Delpire E, Lu J, England R, Dull C, Thorne T. Deafness and imbalance associated with inactivation of the secretory Na-K-2Cl co-transporter. Nature Genetics. 1999;22(2).
81. Lytle C, Xu J-C, Biemesderfer D, Forbush B. Distribution and diversity of Na-K-Cl cotransport proteins: a study with monoclonal antibodies. American Journal of Physiology-Cell Physiology. 1995;269(6):C1496-C505.
82. Hübner CA, Lorke DE, Hermans-Borgmeyer I. Expression of the Na-K-2Cl-cotransporter NKCC1 during mouse development. Mechanisms of Development. 2001;102(1):267-9.
83. Flagella M, Clarke LL, Miller ML, Erway LC, Giannella RA, Andringa A, et al. Mice lacking the basolateral Na-K-2Cl cotransporter have impaired epithelial chloride secretion and are profoundly deaf. Journal of Biological Chemistry. 1999;274(38):26946-55.
84. Ye S, Armah S, Xu Q, Reddy M. Calcein's Quenching In Vitro Method for Assessing Dietary Iron Bioavailability. The FASEB Journal. 2015;29(1 Supplement):LB336.
85. Walker NM, Flagella M, Gawenis LR, Shull GE, Clarke LL. An alternate pathway of cAMP-stimulated Cl− secretion across the NKCC1-null murine duodenum. Gastroenterology. 2002;123(2):531-41.
86. Fejerskov O, Larsen MJ, Richards A, Baelum V. Dental tissue effects of fluoride. Advances in Dental Research. 1994;8(1):15-31.
87. Thylstrup A, Fejerskov O. Clinical appearance of dental fluorosis in permanent teeth in relation to histologic changes. Community Dentistry and Oral Epidemiology. 1978;6(6):315-28.
88. Angmar-Månsson B, Whitford GM. Enamel fluorosis related to plasma F levels in the rat. Caries Research. 1984;18(1):25-32.
89. Lyaruu D, Medina J, Sarvide S, Bervoets T, Everts V, DenBesten P, et al. Barrier formation: potential molecular mechanism of enamel fluorosis. Journal of Dental Research. 2014;93(1):96-102.
90. Den Besten P. Effects of fluoride on protein secretion and removal during enamel development in the rat. Journal of Dental Research. 1986;65(10):1272-7.
91. Clementino-Luedemann TNR, Kunzelmann K-H. Mineral concentration of natural human teeth by a commercial micro-CT. Dental Materials Journal. 2006;25(1):113-9.
92. Everett E, McHenry M, Reynolds N, Eggertsson H, Sullivan J, Kantmann C, et al. Dental fluorosis: variability among different inbred mouse strains. Journal of Dental Research. 2002;81(11):794-8.
93. Kierdorf H, Kierdorf U. Disturbances of the secretory stage of amelogenesis in fluorosed deer teeth: a scanning electron-microscopic study. Cell and Tissue Research. 1997;289(1):125-35.

94. Monsour PA, Harbrow DJ, Warshawsky H. Effects of acute doses of sodium fluoride on the morphology and the detectable calcium associated with secretory ameloblasts in rat incisors. Journal of Histochemistry & Cytochemistry. 1989;37(4):463-71.
95. Smith CE, Nanci A, Denbesten PK. Effects of chronic fluoride exposure on morphometric parameters defining the stages of amelogenesis and ameloblast modulation in rat incisors. The Anatomical Record. 1993;237(2):243-58.
96. Walton R, Eisenmann D. Ultrastructural examination of various stages of amelogenesis in the rat following parenteral fluoride administration. Archives of Oral Biology. 1974;19(2):171IN13179IN5181IN17-178IN4180IN6182.
97. Bronckers A, Jalali R, Lytton J. Reduced protein expression of the Na+/Ca2++ K+-exchanger (Slc24a4) in apical plasma membranes of maturation ameloblasts of fluorotic mice. Calcified Tissue International. 2017;100(1):80-6.
98. Suzuki M, Shin M, Simmer J, Bartlett J. Fluoride affects enamel protein content via TGF-β1-mediated KLK4 inhibition. Journal of Dental Research. 2014;93(10):1022-7.
99. Bronckers A, Wöltgens J. Short-term effects of fluoride on biosynthesis of enamel-matrix proteins and dentine collagens and on mineralization during hamster tooth-germ development in organ culture. Archives of Oral Biology. 1985;30(2):181-91.
100. Franco ÁM, Martignon S, Saldarriaga A, González MC, Arbeláez MI, Ocampo A, et al. Total fluoride intake in children aged 22–35 months in four Colombian cities. Community Dentistry and Oral Epidemiology. 2005;33(1):1-8.
101. Yaeger JA. The effects of high fluoride diets on developing enamel and dentin in the incisors of rats. Developmental Dynamics. 1966;118(2):665-83.
102. Brown W, Eidelman N, Tomazic B. Octacalcium phosphate as a precursor in biomineral formation. Advances in Dental Research. 1987;1(2):306-13.
103. Jälevik B, Odelius H, Dietz W, Norén J. Secondary ion mass spectrometry and X-ray microanalysis of hypomineralized enamel in human permanent first molars. Archives of Oral Biology. 2001;46(3):239-47.
104. Zhou R, Zaki A, Eisenmann D. Morphometry and autoradiography of altered rat enamel protein processing due to chronic exposure to fluoride. Archives of Oral Biology. 1996;41(8-9):739-47.
105. Bronckers A, Lyaruu D, Bervoets T, Wöltgen J. Fluoride enhances intracellular degradation of amelogenins during secretory phase of amelogenesis of hamster teeth in organ culture. Connective Tissue Research. 2002;43(2-3):456-65.
106. João S, Arana-Chavez VE. Tight junctions in differentiating ameloblasts and odontoblasts differentially express ZO-1, occludin, and claudin-1 in early odontogenesis of rat molars. The Anatomical Record Part A: Discoveries in Molecular, Cellular, and Evolutionary Biology. 2004;277(2):338-43.

107. Bronckers AL, Lyaruu DM, Jansen ID, Medina JF, Kellokumpu S, Hoeben KA, et al. Localization and function of the anion exchanger Ae2 in developing teeth and orofacial bone in rodents. Journal of Experimental Zoology Part B: Molecular and Developmental Evolution. 2009;312(4):375-87.
108. Lacruz RS, Nanci A, White SN, Wen X, Wang H, Zalzal SF, et al. The sodium bicarbonate cotransporter (NBCe1) is essential for normal development of mouse dentition. Journal of Biological Chemistry. 2010;285(32):24432-8.
109. Reibring C-G, El Shahawy M, Hallberg K, Kannius-Janson M, Nilsson J, Parkkila S, et al. Expression patterns and subcellular localization of carbonic anhydrases are developmentally regulated during tooth formation. PloS One. 2014;9(5):e96007.
110. Jalali R, Zandieh-Doulabi B, DenBesten P, Seidler U, Riederer B, Wedenoja S, et al. Slc26a3/Dra and Slc26a6 in murine ameloblasts. Journal of Dental Research. 2015;94(12):1732-9.